ORIGINAL PAPER



Wrinkling instabilities for biologically relevant fiber-reinforced composite materials with a case study of Neo-Hookean/ Ogden-Gasser-Holzapfel bilayer

Nhung Nguyen² · Nandan Nath³ · Luca Deseri^{4,5,6,7,8} · Edith Tzeng³ · Sachin S. Velankar^{2,5} · Luka Pocivavsek¹

Received: 30 October 2019 / Accepted: 12 May 2020 © Springer-Verlag GmbH Germany, part of Springer Nature 2020

Abstract

Wrinkling is a ubiquitous surface phenomenon in many biological tissues and is believed to play an important role in arterial health. As arteries are highly nonlinear, anisotropic, multilayered composite systems, it is necessary to investigate wrinkling incorporating these material characteristics. Several studies have examined surface wrinkling mechanisms with nonlinear isotropic material relationships. Nevertheless, wrinkling associated with anisotropic constitutive models such as Ogden–Gasser–Holzapfel (OGH), which is suitable for soft biological tissues, and in particular arteries, still requires investigation. Here, the effects of OGH parameters such as fibers' orientation, stiffness, and dispersion on the onset of wrinkling, wrinkle wavelength and amplitude are elucidated through analysis of a bilayer system composed of a thin, stiff neo-Hookean membrane and a soft OGH substrate subjected to compression. Critical contractile strain at which wrinkles occur is predicted using both finite element analysis and analytical linear perturbation approach. Results suggest that besides stiffness mismatch, anisotropic features associated with fiber stiffness and distribution might be used in natural layered systems to adjust wrinkling and subsequent folding behaviors. Further analysis of a bilayer system with fibers in the (*x*–*y*) plane subjected to compression in the *x* direction shows a complex dependence of wrinkling strain and wavelength on fiber angle, stiffness, and dispersion. This behavior is captured by an approximation utilizing the linearized anisotropic properties derived from OGH model. Such understanding of wrinkling in this artery wall-like system will help identify the role of wrinkling mechanisms in biological artery in addition to the design of its synthetic counterparts.

 $\textbf{Keywords} \ \ Surface \ wrinkling \cdot Ogden-Gasser-Holzapfel \ (OGH) \cdot Artery \cdot Anisotropy \cdot Layered \ systems$

- □ Luka Pocivavsek
 □ lpocivavsek@gmail.com
- Department of Surgery, The University of Chicago, Chicago, USA
- Department of Chemical and Petroleum Engineering, University of Pittsburgh, Pittsburgh, USA
- Department of Surgery, University of Pittsburgh, Pittsburgh, USA
- Department of Civil, Environmental and Mechanical Engineering, University of Trento - Italy, Trento, Italy
- Department of Mechanical Engineering and Materials Science, University of Pittsburgh, Pittsburgh, USA
- Department of Civil and Environmental Engineering, Carnegie Mellon University, Pittsburgh, USA
- Department of Mechanical Engineering, Carnegie Mellon University, Pittsburgh, USA
- Department of Nanomedicine, The Houston Methodist Research Institute, Houston, USA

Published online: 13 June 2020

1 Introduction

Motivated by surface instabilities in natural systems such as arterial wall, skin, brain (Pocivavsek et al. 2018; Genzer and Groenewold 2006; Hohlfeld and Mahadevan 2011), a large amount of research has been performed to understand various modes of surface instabilities such as wrinkling, creasing, and folding in layered materials. Wrinkling is characterized by a smooth surface amplitude undulation (Biot 1963; Allen 1969; Bowden et al. 1998; Pocivavsek et al. 2008; Damman 2015) and is commonly observed on the inner (luminal) surface of arteries (see Fig. 1) (Liu et al. 2014; Svendsen and Tindall 1988; Greensmith and Duling 1984; Pocivavsek et al. 2009). Furthermore, this natural surface pattern often changes as a function of driving forces in the environment, such as the wrinkling and un-wrinkling of arteries with arterial distension due to changes in pressure (see Fig. 1). Recent work of Pocivavsek et al. (2018)

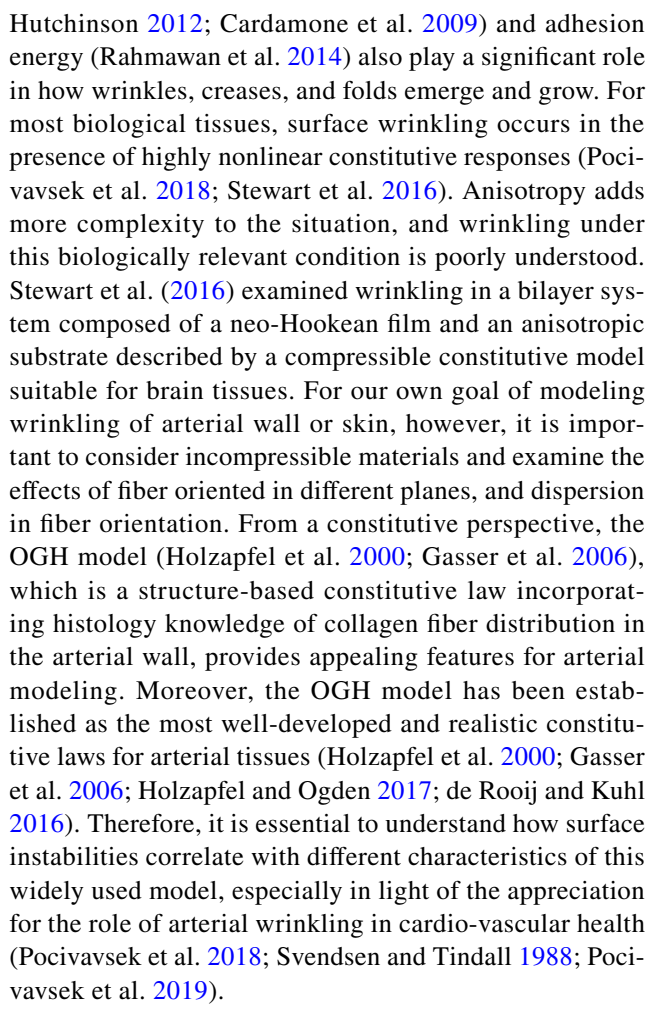


A Mesenteric Artery - Rat Low Pressure High Pressure i. ii. P₂ 20 μm B Carotid Artery - Mouse ii.

Fig. 1 Examples of arterial wrinkling and the actuation of wrinkle amplitude with radial expansion, adapted from Pocivavsek et al. (2018). $\bf a$ i. and $\bf b$ i. show luminal wrinkling and folding at low luminal pressure P_1 . The wrinkle-like topography is sensitive to overall arterial expansion (see $\bf a$ ii.), as seen by the smooth inner surface at higher luminal pressures. $\bf b$ ii. is an FE simulation of the histology derived low-pressure arterial geometry, showing that the pattern can be actuated with expansion

proposed that arterial luminal wrinkling may be used as a mechanical anti-fouling mechanism in arteries. This topography-driven surface renewal (Pocivavsek et al. 2018) is the first model to propose an anti-fouling role for arterial wrinkles.

Various factors that affect the emergence of wrinkling and its transition into folds have been studied for bilayer film-substrate systems subjected to compression. The majority of published literature on buckling of such a system is for isotropic, homogeneous, and linear or weakly nonlinear elastic constitutive models (Sun et al. 2012; Cao and Hutchinson 2012; Brau et al. 2011; Stewart et al. 2016). For a bilayer made from isotropic, elastic materials, such as a neo-Hookean film adhered to a neo-Hookean substrate, the stiffness mismatch of the two layers critically influences the onset of wrinkling and subsequent instability modes at higher compression (Allen 1969; Bowden et al. 1998; Sun et al. 2012; Cao and Hutchinson 2012). Other factors such as pre-stretch (Cao and



This study focuses on wrinkling in a bilayer system composed of a neo-Hookean thin film attached to an OGH substrate. Following the Introduction, Sect. 2 presents experimental data for undulation patterns in pig carotid arteries. The measured wrinkle/fold amplitudes, which follow the square root dependence on strain at high pressures and change to a more linear relationship at low pressures, reveal the need to analyze luminal undulations as interfacial instabilities occurred at different strain levels in arterial wall. Section 3 discusses aspects of the OGH constitutive model that can affect the wrinkling phenomenon. Two solution methods are developed, the analytical perturbation approach and FE analysis, for determining the emergence of wrinkles. Subsequently, the effects of fibers' orientation planes are presented in Sect. 4. Further details on the influence of fiber stiffness and dispersion on the wrinkling strain, wavelength, and amplitude are studied in Sect. 5 by examining a bilayer system under plane strain condition in z direction with fibers lying in the x-y plane, which is parallel to the compression direction (x-axis). An approximation utilizing the linearized orthotropic properties derived from OGH model is also constructed and used to explain the non-monotonic dependence



of the wrinkling strain on fiber orientation. Discussions and suggestions for further work are included in the final section.

2 Arterial wrinkles

As mentioned in the Introduction, many biologic surfaces and in particular arteries show wrinkle-like patterns. However, no biologic study to date has quantitatively shown that these surface patterns indeed follow the well established scalings for amplitude and wavelength for wrinkled bilayers. In general, a bilayer comprising a thin stiff membrane attached to a much thicker, softer substrate under an applied compressive strain ϵ wrinkles with two characteristic length scales: wavelength $\lambda \sim h \times (E_{\rm m}/E_{\rm s})^{1/3}$ and amplitude $A \sim \lambda \sqrt{\epsilon}$, where $E_{\rm m}$ is the membrane modulus, h is membrane thickness, and E_s the substrate modulus (Allen 1969; Bowden et al. 1998; Sun et al. 2012; Cao and Hutchinson 2012). The amplitude scaling follows from the well known inextensibility condition (Genzer and Groenewold 2006; Pocivavsek et al. 2008; Cerda and Mahadevan 2003), i.e., from treating the thin stiff membrane as a layer that can bend but cannot change surface area. Post-wrinkle instabilities, like folding and creasing, are less well understood; however, it has been shown that when bilayers fold, the amplitude scaling changes to a more linear dependence on strain $A \sim \epsilon$ (Pocivavsek et al. 2008).

To explicitly study the amplitude scaling of arteries, pig carotid arteries were harvested from a Pitt Core Animal Facility as per IACUC approved animal protocols. A segment of carotid artery composed of a thin inner elastic lamina (~ 10 µm) and a thicker aterial wall $(\sim 500-600 \,\mu\text{m})$ was then immediately placed on a closed pressurized system prior to any exposure to fixation solution. A saline bag was connected using short tubing to a segment of artery affixed to a catheter tip. The other end of the artery was connected to closed end tubing. Bags were pressurized to a set pressure using a blood pressure cuff. After pressurization, arteries were immediately placed in 2% paraformaldehyde (PFA, Sigma-Aldrich, MO) fixative solution for further processing and imaging. Segments of arteries were pressurized to 40, 60, 80, 100, 120, 140, and 160 mmHg, subsequently fixed, sectioned and imaged under confocal microscopy. Confocal images reveal a continuous undulating internal elastic lamina in a segment of carotid artery that was not distended (see Fig. 2). As the applied pressure increases, the wrinkled topography becomes more flattened across the endothelium. While a nondistended artery has a regular wrinkled appearance, an analogous segment pressurized to 160 mmHg appears flattened without wrinkles. In a non-distended artery, the

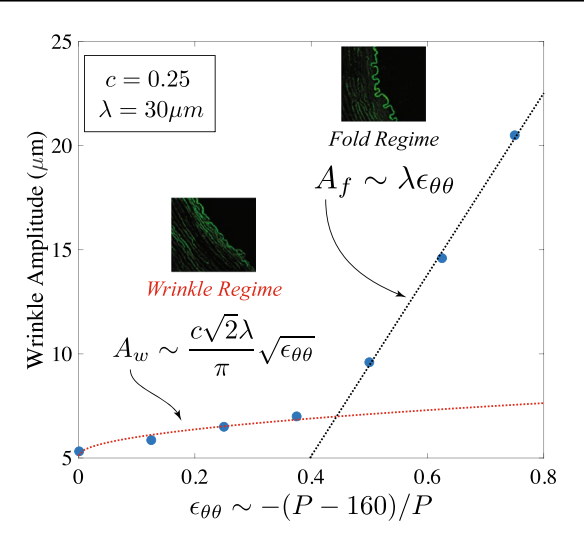


Fig. 2 Experimental data with rat arteries measuring wrinkle amplitude A and wavelength λ as a function of intra-luminal pressure P. Each data point represents the average amplitude of the arterial wrinkles at a given pressure. The fits show that at high pressure (low amplitude wrinkles) A scales linearly with λ and follows a square root dependence on azimuthal compressive strain $\sqrt{\epsilon_{\theta\theta}}$, the canonical wrinkle scaling. At higher compression, lower P, the amplitude scaling becomes linear with strain, a hallmark of post-wrinkle behavior

mean amplitude of wrinkles was $20.58 \pm 0.56\,\mu m$. An artery exposed to 40 mmHg had a similar mean amplitude of $20.52 \pm 0.65\,\mu m$. Amplitude continued to decrease as pressure increased. In a segment pressurized to 160 mmHg, the mean amplitude was $5.32 \pm 0.23\,\mu m$, a reduction of 74%. Mean wavelength of wrinkles at 160 mmHg was $34.36 \pm 1.60\,\mu m$. Wrinkle wavelength remained constant until post-wrinkling folds began to appear with a mean inter-fold distance of $17.32 \pm 0.77\,\mu m$.

Figure 2 plots the wrinkle/fold amplitudes as a function of effective azimuthal compressive strain $\epsilon_{\theta\theta} \sim -(P-160)/P$. The left-hand data points correspond to arteries at highpressure while the right-hand data to arteries at low pressure. Least-squares fits to the data show that at high-pressure, where the luminal topography appears wrinkled, the surface amplitude scales as $A_{\rm w} \sim \lambda \sqrt{\epsilon_{\theta\theta}}$, the well known canonical scaling for bilayer wrinkles (Genzer and Groenewold 2006; Allen 1969; Bowden et al. 1998; Pocivavsek et al. 2008; Cerda and Mahadevan 2003). At lower pressures, higher azimuthal strains, the square root dependence on strain changes to a linear one, which is seen in fold instabilities (Pocivavsek et al. 2008), though precise scaling laws in this post-buckling regime are lacking. These data strongly support the notion that the luminal patterns in arteries are based on a surface instability of a bilayer and may be analyzed accordingly. The second part of this paper focuses on a detailed analysis of wrinkling utilizing a realistic strain energy for the arterial media, the OGH model.



3 Methods

3.1 Constitutive models

A bilayer composed of a thin, stiff, incompressible neo-Hookean film attached to a soft, incompressible OGH substrate is subjected to compression as shown in Fig. 3.

The stiff, incompressible film is described by a neo-Hookean strain energy:

$$W_{\rm NH} = \mu_{\rm f}(\bar{I}_1 - 3) + \frac{1}{D_{\rm f}}(J - 1)^2,\tag{1}$$

where $2\mu_f$ is the shear modulus, K_f is the bulk modulus, $D_f = \frac{2}{K_f}$ is used in numerical implementation to impose (quasi) incompressibility constraint to the film.

For the incompressible substrate, OGH strain energy has the following form (Holzapfel et al. 2000; Gasser et al. 2006):

$$W_{\text{matrix}} = \mu_{\text{s}}(\bar{I}_{1} - 3) + \frac{1}{D_{\text{s}}} \left(\frac{J^{2} - 1}{2} - \ln(J) \right)$$

$$W_{\text{fiber}} = \frac{k_{1}}{2k_{2}} \sum_{\alpha=1}^{N} \left\{ \exp\left[k_{2}\bar{E}_{\alpha}^{2}\right] - 1 \right\}$$

$$W_{\text{OGH}} = W_{\text{matrix}} + W_{\text{fiber}}$$

$$\bar{E}_{\alpha} = \kappa(\bar{I}_{1} - 3) + (1 - 3\kappa)(\bar{I}_{4\alpha\alpha} - 1)$$
(2)

Here, $2\mu_s$ is the shear modulus of the substrate matrix which is described by a neo-Hookean model. K_s is the bulk modulus and $D_s = \frac{2}{K_s}$ is used in the numerical implementation to impose (quasi) incompressibility constraint to the substrate. k_1 is a stress-like parameter associated with fiber stiffness. k_2 is a non-dimensional parameter controlling the nonlinear elasticity of the fibers. N is the number of fiber families with distinct orientations. The invariant $\bar{I}_{4\alpha\alpha} = L_{\alpha}.(\bar{C}L_{\alpha})$ is a pseudo-invariant of the distortion part of the right Cauchy–Green tensor $\bar{C} = \bar{F}^T\bar{F}$ and unit vectors L_{α} in the direction of the αth fiber family. In other words, $\bar{I}_{4\alpha\alpha}$ represents the square of the stretch in the fiber direction α .

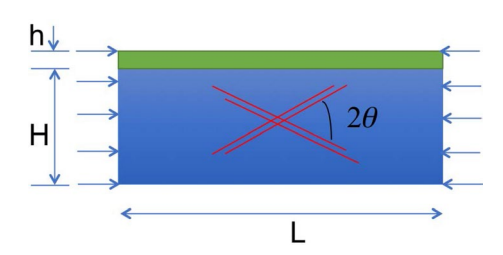
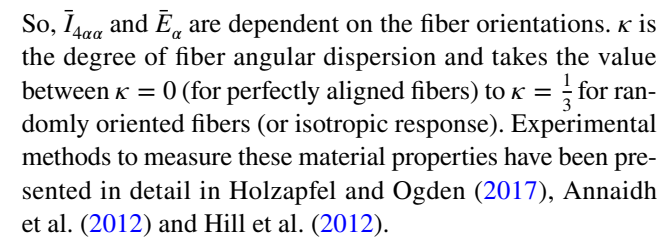


Fig. 3 Thin, stiff, incompressible neo-Hookean film attached to a soft, incompressible OGH substrate with two symmetric families of fibers



The film/substrate modulus mismatch is the primary control parameter for wrinkle onset in isotropic, elastic bilayers (Allen 1969; Bowden et al. 1998; Sun et al. 2012; Cao and Hutchinson 2012; Brau et al. 2011). When the film is much stiffer than the substrate, the wrinkling strain $\epsilon_{\rm w}$ scales with the modulus mismatch as the power law: $\epsilon_{\rm w} \approx \left(\frac{\mu_{\rm s}}{\mu_{\rm c}}\right)^{2/3}$. When the isotropic substrate is replaced by an anisotropic OGH layer, the presence of fibers lead to the effect of additional factors on wrinkling phenomena. In the following sections, three cases of fiber plane orientations (x-y), (x-z), (y-z) as shown in Fig. 4 are considered to explore the effects of fiber stiffness k_1 , fiber orientation θ , and fiber dispersion κ . A plane strain condition in the z direction is assumed, and two solution approaches (linear perturbation and FE) are developed to analyze the wrinkling phenomena. Three limiting cases (fibers oriented in either x, y or z direction) are also presented and discussed in detail.

3.2 Linear perturbation approach

Linear perturbation has proved to be an efficient technique in determining the onset of wrinkling in isotropic systems (Biot 1963; Sun et al. 2012; Cao and Hutchinson 2012). A recent work (Stewart et al. 2016) extended the technique to analyze the wrinkling onset for a bilayer composed of a compressible fiber-reinforced substrate and a neo-Hookean thin film. Here, the technique is applied to analyze the neo-Hookean film/OGH substrate bilayer in Figs. 3 and 4 with the incompressibility consideration for the materials in both layers. In particular, starting with the uniform, plane strain deformation state described in Eq. 3, a perturbation of this homogeneous deformation with the generic forms of perturbation shown in Eq. 4 for the case of incompressibility (Sun et al. 2012) is applied to both the film and the substrate.

Homogeneous deformation state is specified as:

$$x = \lambda_x X$$

$$y = \frac{1}{\lambda_x} Y$$
(3)

where (X, Y) are coordinates in the undeformed configuration and (x, y) are the corresponding coordinates in the current configuration. λ_x is the lateral stretch in the x direction.

A perturbation is applied with incompressibility constraint:



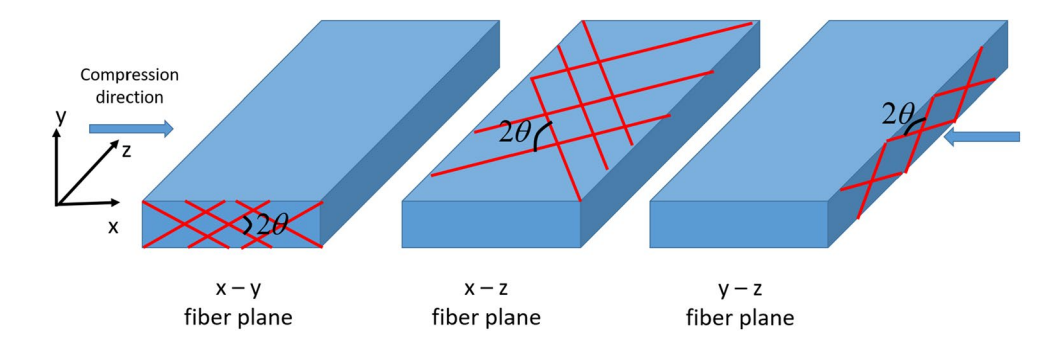


Fig. 4 Two fiber families lying in three planes (x-y), (x-z), (y-z) in the OGH substrate. Compression is in the x direction and plane strain condition in z direction are assumed. The fiber angle θ is defined with respect to different axes depending on the fiber plane. Three limiting

cases are: fibers aligned in x direction (i.e, $\theta = 0^{\circ}$ in (x-y) and (x-z) planes), fibers aligned in y direction (i.e, $\theta = 90^{\circ}$ in (x-y) plane and $\theta = 0^{\circ}$ in (y-z) plane), fibers aligned in z direction (i.e, $\theta = 90^{\circ}$ in (y-z) and (x-z) planes)

$$x = \lambda_x X - \alpha \delta \lambda_x^2 \lambda \sin(kX) e^{\alpha kY}$$

$$y = \frac{1}{\lambda_x} Y + \delta \lambda \cos(kX) e^{\alpha kY}$$

$$p = p_0 + \delta p_1 \cos(kX) e^{\alpha kY}$$
(4)

where $\delta << 1$ is the perturbation amplitude parameter. $k=\frac{2\pi}{\lambda}$ is the wrinkle wave number, λ is the undeformed-configurational wavelength of the perturbation. α is a parameter to be determined from the equilibrium condition. p is the hydrostatic pressure for incompressible solids. p_0, p_1 are to be determined from boundary conditions.

For each layer, substituting the prescribed constitutive models in Sect. 3.1 and the perturbed deformation state in Eq. 4 into the equilibrium equations, a fourth-order equation for α is obtained. Four solutions of α are used to construct four eigenmodes for the film. While for the substrate, the undulation must disappear as $Y \to -\infty$. Here, Y = 0 corresponds to the interface between the film and the substrate. Due to this requirement, two solutions of α with the negative values for the real part can be neglected. Thus, only two solutions of α and correspondingly two eigenmodes for the substrate are considered.

In the bilayer system, the deformation state of each layer due to the above perturbation is a linear combination of its corresponding eigenmodes. A total of 6 parameters (4 for the film and 2 for the substrate), therefore, are needed in the linear combinations for the film and substrate. They are then substituted into a total of 6 continuity and boundary conditions (normal, tangential displacement continuities, and normal, tangential traction continuities at the interface; free normal and tangential tractions on the top of the film). This results in an eigenvalue problem of the form $f(\lambda_x, kh) = 0$ to determine the wrinkling strain ϵ_w . Here, f is the determinant of the system of 6 equations constructed from continuity and boundary conditions and is a nonlinear function in terms of the applied stretch λ_x and the product of wave number k and

film thickness *h*. The eigenvalue problem is solved numerically and the critical stretch is the one that minimizes overall *kh* values. Detailed derivations for this linear perturbation procedure are provided in "Appendix 1."

3.3 Finite element (FE) analysis

The wrinkling strain, wavelength, and amplitude are also determined using FE analysis. FE simulations are implemented using the commercial software package Abaqus v6 .18 (Dassault-Systemes Simulia Inc., Providence, RI 2018) with the dynamic explicit solver. For fiber plane (x-y), two-dimensional plane strain elements (CPE4R, 4-node bilinear, reduced integration with hourglass control) are used to model both the film and the substrate. For the (x-z) and (y-z) planes, three-dimensional elements (C3D8R, 8-node linear brick, reduced integration, with hourglass control) are used as the 2D settings were not able to capture the effects of the fibers in the z-directions. However, an effective plane strain condition is still imposed by applying the displacement constraints in the z direction.

With the assumption that fibers bear no compressive load, the built-in OGH model in Abaqus deactivates the contribution of fibers, which are under compression, to the strain energy. Here, an Abaqus material subroutine VUMAT for the OGH substrate without this assumption is also implemented in order to test the effect of this deactivation on wrinkling phenomenon.

For both analytical and FE methods, the following sets of material and geometric parameters are utilized. The ratio H/h between the depth of the substrate and the thickness of the film is taken to be more than 50 to ensure that the substrate is sufficiently deep to be treated as a half-space. The original length of the bilayer L is also set to be much larger than the thickness h of the film: $L \approx 200h$. The shear modulus μ_s and the fiber nonlinearity parameter k_2 for the OGH substrate are adopted from a calibrated example for arterial



wall in Holzapfel and Ogden (2017), specifically, $\mu_s = 3000$ Pa, $k_2 = 0.8393$. The parameter $D_s = 1.6 \times 10^{-5}$ Pa⁻¹ is selected to ensure quasi-incomressibility in FE analysis as suggested in ABAQUS (2018). Other parameters k_1 (fiber stiffness), κ (fiber dispersion), θ (fiber orientation) are varied to study how they influence ϵ_w . For the neo-Hookean film, a shear modulus value of $\mu_f = 307,500$ Pa, and correspondingly $D_f = 1.626 \times 10^{-7}$ Pa⁻¹, is selected which is approximately 100 times stiffer than the shear modulus μ_s of the substrate matrix. It is noted here that the analysis presented in this paper is also applicable to other cases of μ_f/μ_s ratio, but a specific ratio is considered here in order to reduce the parameter space and have a more detailed analysis of the contribution of fibers on wrinkling and folding phenomena.

4 Effects of fiber plane on $\varepsilon_{\rm w}$ of bilayer system composed of a thin, stiff neo-Hookean layer on an OGH substrate

In the absence of the fibers, the situation corresponds to a neo-Hookean film bonded to a neo-Hookean substrate with a modulus mismatch of 100. For this case, FE and analytical perturbation analyses predict the wrinkle strain of 0.023, which is designated as $\epsilon_{\rm NH}$. In the presence of fibers, consider three cases of fiber plane orientations (x-y), (x-z), (y-z) with the assumption of a plane strain condition in the z direction as shown in Fig. 4. Two families of fibers are assumed to be perfectly aligned along directions $\pm \theta$, i.e., $\kappa = 0$. The effects of fiber dispersion will be discussed in Sect. 5. $\epsilon_{\rm w}$ is determined by the two approaches which are outlined in the method section. Figures 5, 6 and 7 show the critical strain for

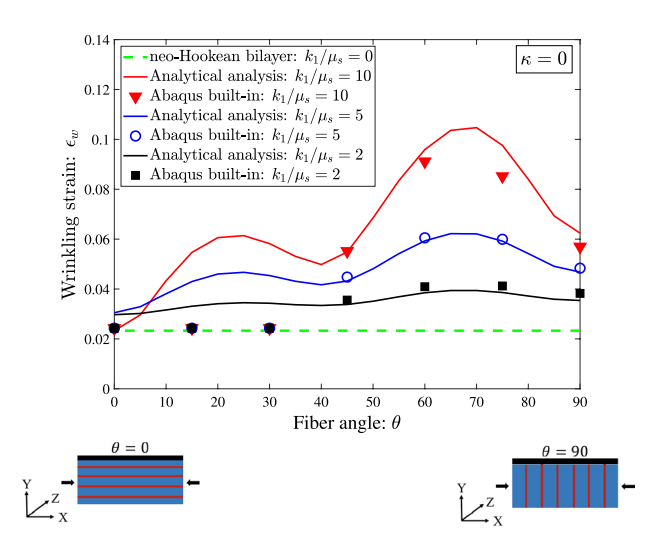


Fig. 5 $\epsilon_{\rm w}$ for the case in which fibers are lying in (x-y) plane. The markers indicate predictions by the built-in OGH in Abaqus. Note that the triangles, squares, and circles overlap at small angles

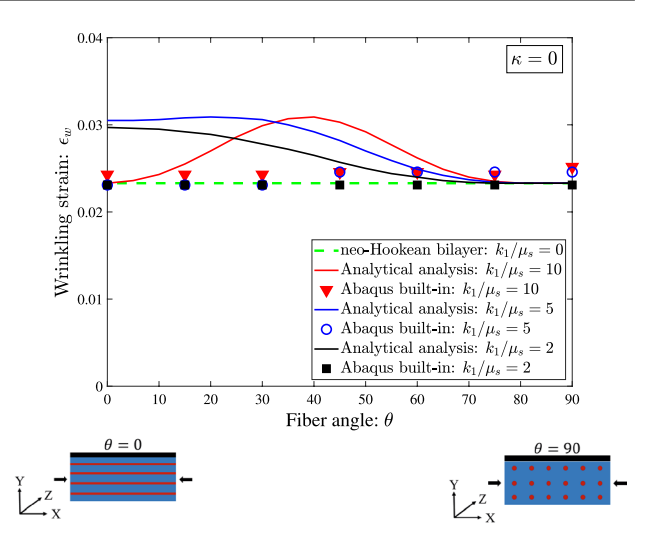


Fig. 6 $\epsilon_{\rm w}$ for the case in which fibers are lying in (x–z) plane. The markers indicate predictions by the built-in OGH in Abaqus. $\epsilon_{\rm w}$ for $\theta=0^{\circ}$ in (x–z) plane here are in agreement with $\epsilon_{\rm w}$ for $\theta=0^{\circ}$ in (x–y) plane presented in Fig. 5, which are for the limiting case where fibers are perfectly aligned in x-direction

wrinkling $\epsilon_{\rm w}$ with varying fiber stiffness and orientations as fibers lie in (x-y), (x-z) and (y-z) planes, respectively. The small schematics under each graph in Figs. 5, 6 and 7 show how the fiber alignment varies as θ changes from 0° to 90°. All three figures show that when fiber stiffness $k_1 = 0$, the response expected from a neo-Hookean bilayer is obtained in three fiber planes.

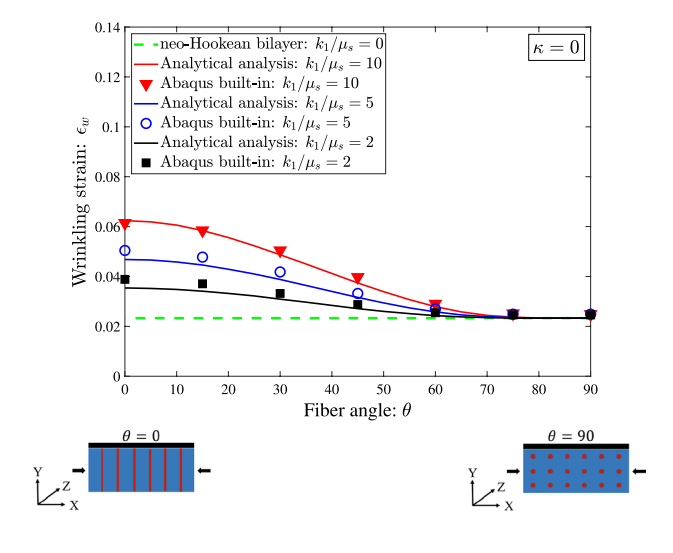


Fig. 7 $\epsilon_{\rm w}$ for the case in which fibers are lying in (y-z) plane. The markers indicate predictions by the built-in OGH in Abaqus. $\epsilon_{\rm w}$ for $\theta=0^{\circ}$ and $\theta=90^{\circ}$ in (y-z) plane here are in agreement with $\epsilon_{\rm w}$ for $\theta=90^{\circ}$ in (x-y) plane and $\theta=90^{\circ}$ in (x-z) presented in Figs. 5 and 6, which are for the limiting cases where fibers are perfectly aligned in y-direction and z-direction, respectively



 $\epsilon_{\rm w}$ predicted from FE analysis using the built-in OGH model in Abaqus are in good agreement with the predictions of linear perturbation analysis for the case of (y-z) fiber plane (see Fig. 7). For fibers oriented in (x-y) plane (Fig. 5), similarly good agreement is obtained for high fiber angles $(\theta \ge 45^{\circ})$. However, for angles below 45° in Fig. 5, the builtin OGH model predicts $\epsilon_{\rm w} = 0.023 = \epsilon_{\rm NH}$, independent of the orientation or fiber modulus. This indicates that fibers do not alter wrinkling onset in these cases. On the other hand, the linear perturbation analysis at these low fiber angles shows a non-monotonic dependence of ϵ_{w} on fiber angle θ . Figure 6 also demonstrates such a deviation between the built-in OGH in Abagus and our analytical analysis when fibers are oriented close to compression direction ($\theta \to 0^{\circ}$). The reason for these discrepancies is that fibers are subjected to compression under these situations and the built-in OGH model in Abagus deactivates their contribution to the strain energy (Gasser et al. 2006; ABAQUS 2018), while our analytical analysis allows for anisotropic fiber-reinforcement in compression (Brangwynne et al. 2006; Fraldi et al. 2019; Ciarletta et al. 2011). To further verify this, in Sect. 5, the results for a VUMAT subroutine for OGH model, but relaxing this assumption, show good agreements with the analytical approach even at low fiber angles. It is also noted that when the fiber stiffness becomes very large, some differences in the predicted ϵ_{w} of these two approaches are observed such as at $\frac{k_1}{\mu_k} = 10$, $\theta = 75^{\circ}$ in Fig. 5. However, even for these extreme cases, the trend of $\epsilon_{\rm w}$ with respect to the fiber orientation and fiber stiffness is consistent between FE and linear perturbation analyses.

The orientation planes of the fibers strongly affect $\epsilon_{\rm w}$. For fibers in (x-y) and (x-z) planes, if the fibers are oriented closer to the axis of compression, meaning $\theta \approx 0^{\circ}$, increasing fiber stiffness can lead to either an increase or decrease in $\epsilon_{\rm w}$. For example, in the (x-z) fiber plane, when $\theta=0^{\circ}$ (i.e, fibers aligned in x-direction), $\epsilon_{\rm w}$ increases when k_1 increases from 6000 to 15,000 Pa, but reduces at $k_1 = 30,000$ Pa. The results also correspond to the case of $\theta = 0^{\circ}$ in the (x-y) plane (again, fibers aligned in x-direction) as shown in Fig. 5. However, for fibers in (y-z) plane, a monotonic increase in $\epsilon_{\rm w}$ is observed when the fiber stiffness increases. Furthermore, $\epsilon_{\rm w}$ shows a non-monotonic behavior with respect to the fiber inclination in the (x-y) plane. The nonmonotonic dependence on fiber angle for (x-y) fiber plane was also reported by Stewart et al. (2016) but unlike the non-monotonic shape that they found (see Fig. 4 in Stewart et al. 2016), here two local maxima of $\epsilon_{\rm w}$ for a specific level of fiber stiffness k_1 were obtained (Fig. 5). On the other hand, for fibers lying in (y-z), the behavior is monotonic (Fig. 7).

Figures 6 and 7 also indicate that if fibers are oriented close to the z-axis (i.e, $\theta \to 90^{\circ}$), they have insignificant effect and $\epsilon_{\rm w}$ approaches $\epsilon_{\rm NH}$. However, as fibers are oriented

away from z-axis, $\varepsilon_{\rm w}$ increases, indicating that wrinkling becomes more difficult. Among the three planes investigated here, the (x-z) plane response shows less significant effect on $\varepsilon_{\rm w}$. This might be due to the assumption of plane strain in the z-direction. For (x-z) and (y-z) configurations, a coupling in the z-direction departs the analysis from a 2D analysis which is also observed in the FE analysis using 2D and 3D settings. In addition, for these two configurations, plane strain in the z-direction means that a compressive stress develops to maintain zero strain in the z direction. Thus, very stiff fibers could promote buckling in that direction. Therefore, it would be interesting to extend the analysis here to investigate these configurations with a general 3D setting.

5 The influence of fiber stiffness, orientation and dispersion on wrinkling

In order to further investigate the effects of fibers' stiffness, orientation, dispersion on wrinkling, we analyze the (x-y) fiber orientation in more detail.

5.1 Wrinkling strain $\epsilon_{\rm w}$

5.1.1 Fiber dispersion κ

 $\epsilon_{\rm w}$ for $\kappa=0$ (i.e., perfectly aligned fibers) is already presented in Fig. 5 of Sect. 4. For more dispersed fiber distributions, the dependence of $\epsilon_{\rm w}$ on fiber angle θ at different values of fiber stiffness k_1 is presented in Fig. 8 for $\kappa=0.133$ and $\kappa=0.226$.

All cases show reasonable agreements between FE and analytical analyses. Again, $\epsilon_{\rm w}$ is found to change non-monotonically with fiber angle. $\epsilon_{\rm w}$ values at $\theta=45^{\circ}$ and $\theta=90^{\circ}$ are less than the values for $\theta=60^{\circ}$ and $\theta=75^{\circ}$. As κ approaches 1/3, which corresponds to a more isotropic distribution of fibers, the discrepancy between different fiber angles and stiffness values becomes smaller. As expected, Fig. 8 shows that $\epsilon_{\rm w} \to \epsilon_{\rm NH}$ as $\kappa \to \frac{1}{3}$.

5.1.2 Fiber reinforcement in compression

As pointed in Sect. 4, at low fiber angles θ with respect to the compression direction (x-axis), the built-in OGH model deviates from the linear analysis due to the assumption that fiber bears no compressive load. Here, a comparison between FE approach using a VUMAT material subroutine that relaxes this assumption in ABAQUS and linear perturbation analysis is shown in Fig. 9. Good agreement between VUMAT predictions and analytical predictions indicates that permitting the fiber to bear compressive stress leads to a significant increase in $\epsilon_{\rm w}$ for certain values of fiber angles such as 30°, 15°. Specifically, an increase from 0.0233 (fiber



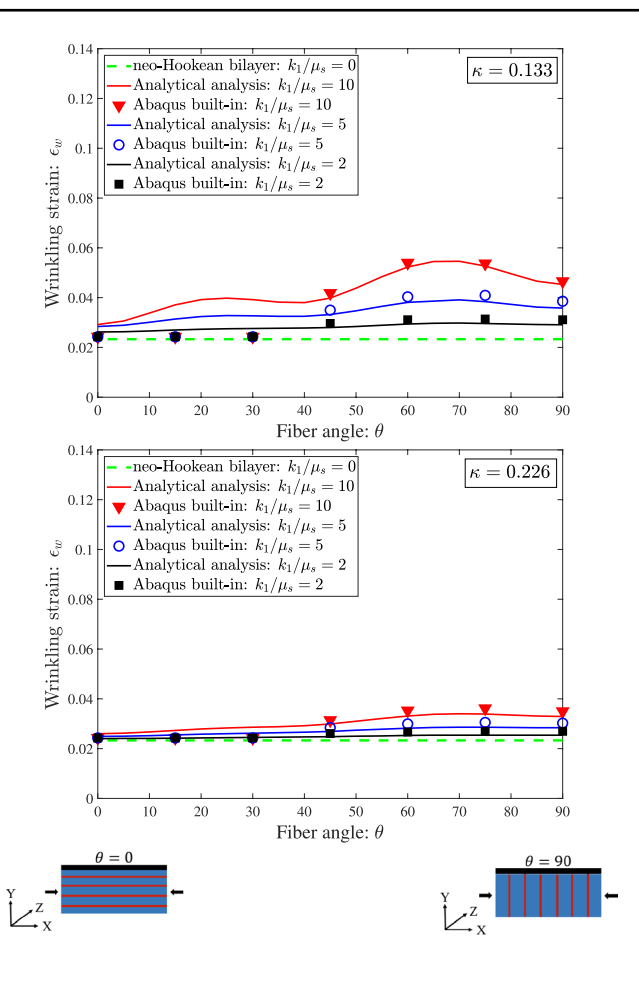


Fig. 8 $\epsilon_{\rm w}$ for different fiber dispersion κ values in (x-y) fiber plane. The schematics at the bottom show the mean fiber orientation at $\theta=0^{\circ}$ and $\theta=90^{\circ}$

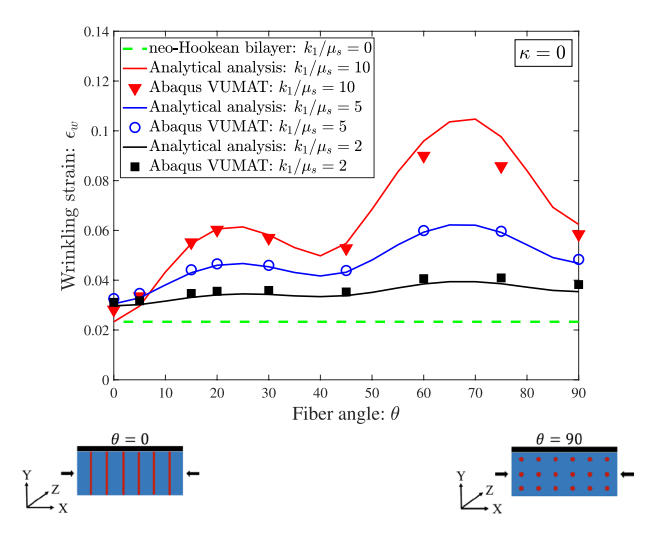


Fig. 9 $\epsilon_{\rm w}$ for the case of fiber dispersion $\kappa=0$ in (x-y) fiber plane. Abaqus VUMAT in which fiber compression is not deactivated shows good agreement with analytical approach even at low fiber angles θ

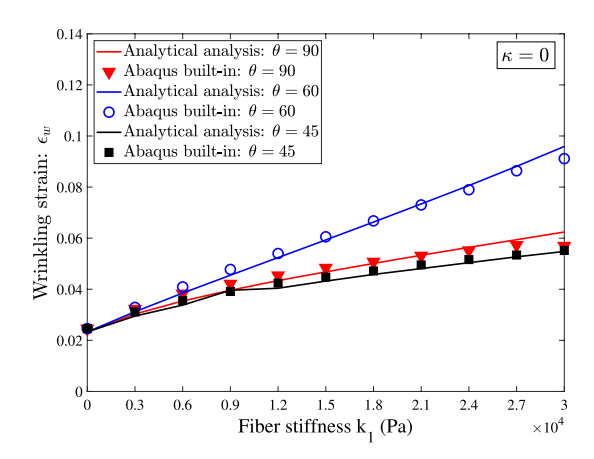


Fig. 10 $\epsilon_{\rm w}$ versus fiber stiffness k_1 for the case of fiber dispersion $\kappa=0$ in (x-y) fiber plane

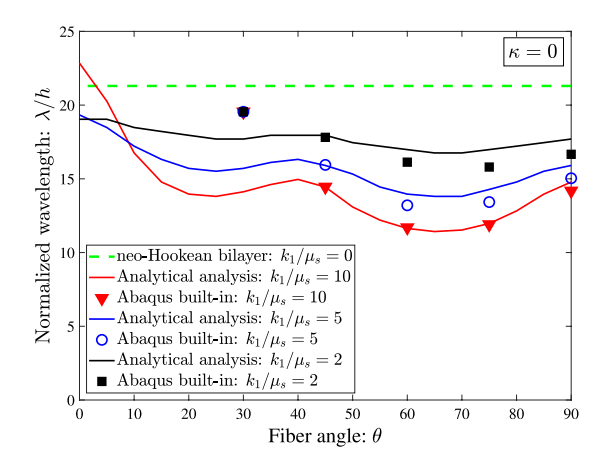


Fig. 11 Wrinkling wavelength versus fiber angle θ for the case of fiber dispersion $\kappa = 0$ in (x-y) fiber plane

bears no compressive stress) to 0.06 (fiber bears compressive stress) is found for $\epsilon_{\rm w}$ at $k_1=30{,}000~{\rm Pa}$ and $\theta=30^{\circ}$.

5.1.3 Fiber stiffness k_1

The effects of fiber stiffness on $\epsilon_{\rm w}$ at certain values of fiber angle θ are shown in Fig. 10. We focus this parameter sweep to three angles $\theta = 45^{\circ}$, 60° , and 90° degrees. A monotonic increase in $\epsilon_{\rm w}$ with respect to fiber stiffness k_1 is observed.

5.2 Wavelength and amplitude

Besides the onset of wrinkling, wavelength, and amplitude are important features of the wrinkling pattern. Here, the normalized wavelength λ/h , where h is the film thickness, is plotted in Fig. 11. This normalized wavelength is related to the dimensionless wavenumber k as: $\frac{\lambda}{h} = \frac{2\pi}{kh}$.

The wavelength also exhibits a non-monotonic behavior with respect to the fiber angle θ . The change in the



wavelength is not as significant as for $\epsilon_{\rm w}$, though for certain fiber angle and stiffness combination, a decrease factor of 2 in the wavelength can be observed as compared to the neo-Hookean bilayer.

After wrinkles emerge, wrinkle amplitude grows with the increasing applied strains as shown in Fig. 12. Here, wrinkle amplitude is calculated as the deviation from the mean surface height at each strain level by tracking back the evolutions of two folds and the nearest and global maxima between them. The data also clearly show that in the wrinkle regime, amplitude follows the canonical square root

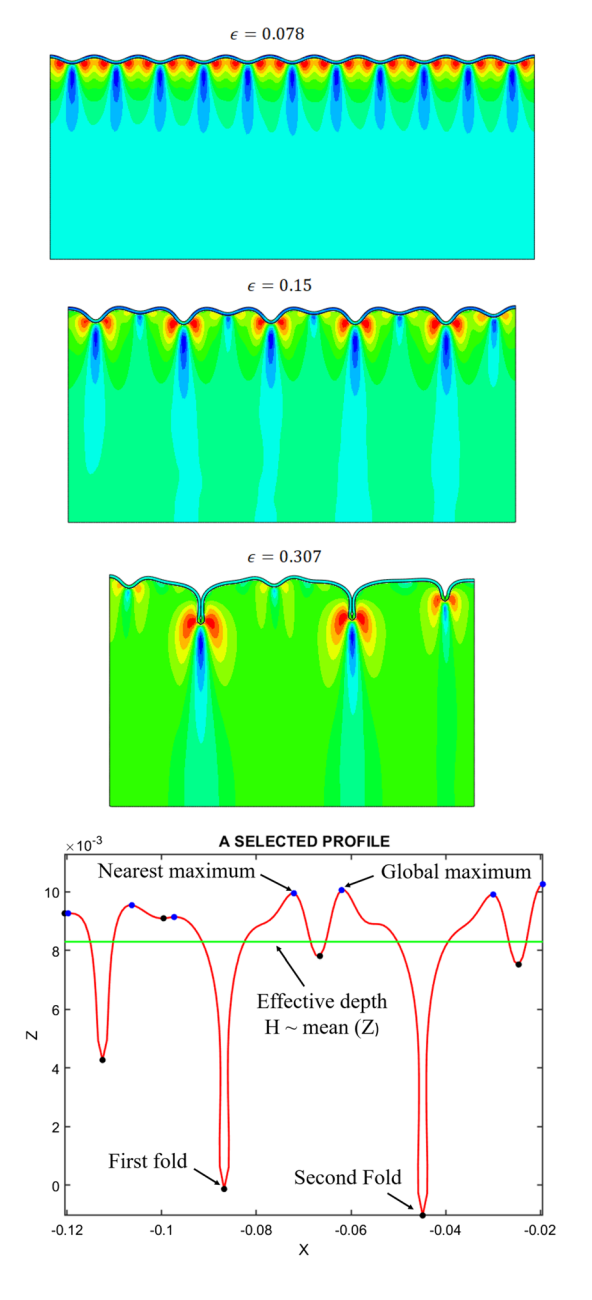


Fig. 12 Wrinkle and transition to period doubling and folding in (x-y) fiber plane, fiber angle $\theta = 90^{\circ}$, fiber stiffness $k_1/\mu_s = 2$

dependence on the strain beyond $\epsilon_{\rm w}$: $A \approx \lambda \sqrt{\frac{\epsilon - \epsilon_{\rm w}}{\epsilon_{\rm w}}}$ as shown in Fig. 13.

6 Discussion

Geometry and geometric instabilities are ubiquitous at natural interfaces (Genzer and Groenewold 2006; Hohlfeld and Mahadevan 2011; Pocivavsek et al. 2008, 2019; Cerda and Mahadevan 2003). Often the mechanisms that lead to the beautiful array of surface buckling, wrinkling, folding, and creasing can be understood from the vantage of elasticity involving little if any biology; indeed, this approach has led to scaling laws predicting the onset and dominant lengths scales in arterial wrinkling (Pocivavsek et al. 2009), brain sulcus formation (Hohlfeld and Mahadevan 2011), and skin wrinkles (Cerda and Mahadevan 2003; Puntel et al. 2011; Cerda 2005). This literature has focused on the universality of the wrinkle instabilities and as such the elasticity problem is often solved in a reduced form where the nonlinearities appear from the geometry alone, and the constitutive response is limited to linear elasticity (Pocivavsek et al. 2009). This approach correctly captures the general wrinkling instability for composite bilayer systems. However, the need for a more detailed and tissue specific analysis has arisen in the last several years (Stewart et al. 2016), particularly driven by the growing appreciation that these patterns influence the functional biology of the given tissue (Pocivavsek et al. 2018, 2019; Shivapooja et al. 2013; Shyer et al. 2013; Ciarletta et al. 2014) and the desire to build this bio-functionality into medical devices (Pocivavsek et al. 2018, 2019; Yang et al. 2010; Epstein et al. 2013; Hasan and Chatterjee 2015; Levering et al. 2014; Chen et al. 2011; Mao et al. 2009). Our work has focused on arterial wrinkling and folding, and we have hypothesized that these patterns could be used by native arteries as a biomechanical strategy to prevent unwanted platelet adhesion (Pocivavsek et al. 2009, 2018, 2019). In the first part of this paper, we show that arterial wrinkling is a dynamic instability that follows the canonical (Genzer and Groenewold 2006; Hohlfeld and Mahadevan 2011; Pocivavsek et al. 2008, 2019; Cerda and Mahadevan 2003) scalings of wrinkle mechanics; in particular, the amplitude at low compressive strain scales linearly with wavelength and as the square root of the strain. This point has not been shown in the literature thus far and is an important experimental validation of the elasticity approaches often used to describe these biologic patterns. Furthermore, the change in surface amplitude with luminal pressure demonstrates that arterial topography is sensitive to intra-arterial pressure making plausible that topography actuation is a biologically relevant surface renewal strategy as hypothesized previously (Pocivavsek et al. 2018, 2019).



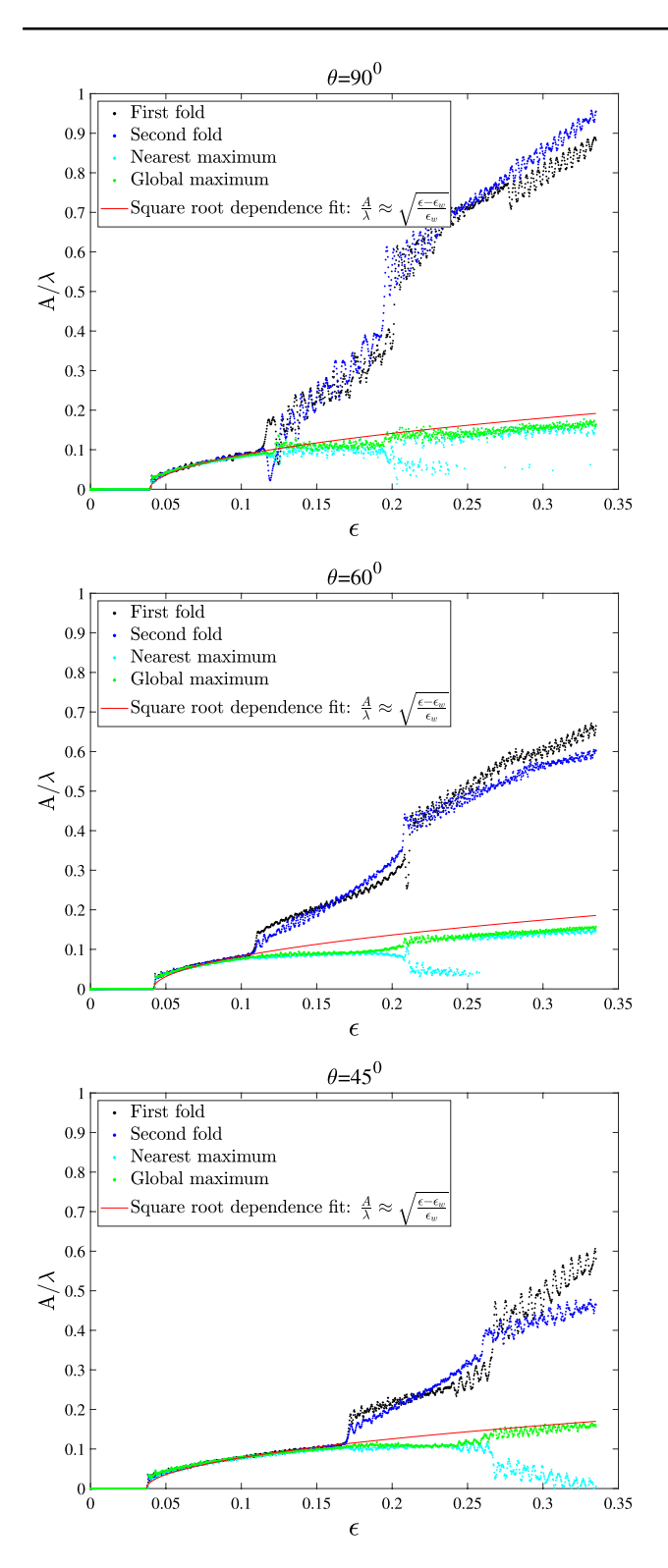


Fig. 13 Wrinkle amplitude for three fiber angles $\theta = 90^\circ, 60^\circ, 45^\circ$ with respect to *x*-axis in (x-y) fiber plane for the case of fiber stiffness $k_1/\mu_s = 2$. Red line is a fit to $A/\lambda = c\sqrt{\frac{\varepsilon - \varepsilon_w}{\varepsilon_w}}$ where c is a fitting parameter. The fittings indicate that wrinkle amplitude grows with the square root of the normalized applied strain

The second part of this paper focuses on a detailed computational and analytical analysis of the wrinkle instability in a model bilayer where the substrate material response is modeled using the well validated OGH arterial constitutive law. Our work presents a detailed study of the influences of several features in the OGH model on the wrinkling behavior. We study the response utilizing both the built-in OGH function in Abaqus, a more general implementation via a VUMAT that allows for fiber bearing compressive loads, and a purely analytical approach using linear perturbation analysis. The three approaches overall give similar results for $\epsilon_{\rm w}$, validating that the correct physics has been captured. In all three cases, we chose to model only the substrate using OGH. The substrate anatomically corresponds to the thick arterial media which is rich in collagen, elastin, and smooth muscle cells (Holzapfel et al. 2000; Gasser et al. 2006). The arterial media is also most prone to disease formation such as atherosclerosis or thickening due to years of high cholesterol and high blood pressure (Sidawy and Perler 2018). As such, we elected to focus the increase in complexity in material response onto the media. The thinner stiffer part of the artery that acts as the film or membrane in the wrinkling bilayer is often taken to be composed of both the endothelium and internal elastic lamina (IEL) (Pocivavsek et al. 2009). In this paper, we utilize a neo-Hookean constitutive response for the IEL/endothelium layer in order to reduce the already large parameter space of the problem; furthermore, while this condition could be relaxed, prior work on wrinkling has shown that the membrane undergoes primarily bending dominated deformations and is often treated as inextensible and linearly elastic with little loss of generality (Allen 1969; Pocivavsek et al. 2008; Cerda and Mahadevan

6.1 Impact of fiber angle and orientation on $\epsilon_{\rm w}$

2003).

The fibers in the OGH model represent collagen, which in a straight segment of artery is thought to wrap around the long axis of the artery in helical fashion (Holzapfel et al. 2000; Gasser et al. 2006). However, collagen orientation becomes distorted in many disease states and is poorly understood at bifurcations and along curved arterial segments, corresponding to areas of the arterial tree most prone to disease. The approach in this paper was to study the effect of fiber orientation (θ) in all three planes independently, as shown in Fig. 4. Our main results in Figs. 5, 6 and 7 show that $\epsilon_{\rm w}$ is highly sensitive to θ and the fiber orientation plane. Fibers oriented in the x-y plane show the greatest impact on $\epsilon_{\rm w}$ as a function of θ and fiber stiffness, followed by fibers oriented in the y-z plane. The least impact is exerted by fibers in the x–z plane. One way to interpret the impact of fiber orientation on wrinkling is to analyze the relative orientation



of the fibers with respect to the two primary directions of displacement in the problem: direction of compression (x) and direction of amplitude growth (y).

Case 1 is fibers oriented purely along z and thus orthogonal to both direction of compression and amplitude growth, which is achieved for $\theta=90$ in Figs. 6 and 7. In this case, the fibers are effectively removed from the elastic response of the substrate as it concerns wrinkling, which is shown in our data by $\epsilon_{\rm w} \Rightarrow \epsilon_{\rm NH}$. The other two limiting cases represent fibers oriented in either the direction of compression (case two) or amplitude growth (case three).

Case 2 is achievable for fibers oriented in the x-y and x-z planes for $\theta=0$ (note the same $\epsilon_{\rm w}$ for this angle in Figs. 5 and 6). Case 3 is achievable for fibers oriented in the x-y plane at $\theta=90$ and fibers in the y-z plane for $\theta=0$ (again, $\epsilon_{\rm w}$ is identical at these angles in Figs. 5 and 7).

Case 3 is simplest to understand physically. The fibers behave as extra springs in the direction of amplitude growth, effectively stiffening the substrate response along this direction, which is seen in the increasing $\epsilon_{\rm w}$ with increasing fiber stiffness. Case 2 shows that fibers oriented purely along the direction of compression perturb the onset of wrinkling far more weakly compared to case 3. These results show that the substrate elastic response in the two limiting cases of fiber orientation, irrespective of fiber plane, is most sensitive to perturbations along the direction of amplitude growth. This is consistent with well known elasticity approaches for wrinkling in bilayer systems, where the substrate is often treated as a simple potential acting normal to the interface (Pocivavsek et al. 2008) or spring-like Winkler foundation (Damman 2015; Cerda and Mahadevan 2003).

6.2 Approximation based on linearized orthotropic properties—case study of fibers in the *x*–*y* plane

For plane strain, isotropic, and incompressible bilayers with high modulus mismatch $\mu_{\rm f}/\mu_{\rm s}$, and in the absence of prestrain, the wrinkling strain and wavelength are approximated as follows (Sun et al. 2012; Cao and Hutchinson 2012; Brau et al. 2011):

$$\epsilon_{\rm w} \approx \frac{1}{4} \left(\frac{3\mu_{\rm s}}{\mu_{\rm f}} \right)^{2/3}, kh \approx \left(\frac{3\mu_{\rm s}}{\mu_{\rm f}} \right)^{1/3}$$
 (5)

Thus, $\frac{(kh)^2}{\epsilon_w}$ is approximately equal to 4. This ratio for bilayers of a neo-Hookean film bonded to an orthotropic OGH substrate, however, shows deviations from this constant trend (Fig. 16, "Appendix 2").

Equivalent relationships have also been derived in the literature for wrinkling in sandwich panels. Vonach and Rammerstorfer (2000) provides the following approximation in

which $\epsilon_{\rm w}$ depends on the core's transverse stiffness $E_{\rm y}^{\rm c}$ and shear modulus $G_{\rm vol}^{\rm c}$.

$$\epsilon_{\rm w} \approx 0.85 \left(\frac{E_y^{\rm c} G_{xy}^{\rm c}}{E_{\rm f}^2}\right)^{1/3}$$
 (6)

A further analysis in Vonach and Rammerstorfer (2000) indicates that the orthotropic core's longitudinal stiffness E_x might also influence ϵ_w .

For the OGH model, the stiffnesses E_x , E_y , E_z , shear moduli G_{xy} , G_{yz} , G_{xz} , and Poisson's ratios v_{xy} , v_{yx} , v_{zz} , v_{zx} , v_{yz} , v_{zy} , and be derived through linearization (see "Appendix 2"). They are complex functions of fiber stiffness k_1 and angle θ . Specifically, E_x and E_y depend nonlinearly and non-monotonically on θ with a local minimum at the "magic angle" (Goriely 2017) $\theta \approx 55^\circ$ and $\theta \approx 35^\circ$, respectively (Fig. 17, "Appendix 2"). Here, a similar combination of these quantities as in Eq. 6 is constructed with an attempt to explain and correlate with the observed non-monotonic behavior in ϵ_w :

$$\epsilon_{\rm w} \approx 0.85 \left(\frac{E_{\rm eff}^{\rm s} G_{xy}^{\rm s}}{E_{\rm f(eff)}^2}\right)^{1/3}, E_{\rm eff}^{\rm s} \approx \frac{\sqrt{E_x E_y}}{1 - v_{xz} v_{zx}}$$
 (7)

where the film's effective modulus under the condition of plane strain and incompressibility is $E_{\rm f(eff)} = \frac{E_{\rm f}}{1-v_{\rm f}^2} = \frac{E_{\rm f}}{0.75}$. The substrate's effective modulus $E_{\rm eff}^{\rm s}$ is assumed to depend on both the longitudinal and transverse stiffnesses E_x , E_y as suggested in Vonach and Rammerstorfer (2000).

The good agreement in Fig. 14 between the linear perturbation analysis and the derived approximation for various fiber dispersion values suggests that $\epsilon_{\rm w}$ may be predicted from the longitudinal, transverse, and shear moduli and Poisson's ratio in certain directions of the OGH substrate. Nevertheless, refinements are needed to obtain a universal effective stiffness for the substrate that can be applicable to different fiber planes and stiffness mismatch ratios and, possibly, in the presence of pre-strain. The limit $\mu_{\rm f} >> k_1 >> \mu_{\rm s}$ can be further explored to gain better insight into the new scaling law that is similar to Eqs. 5 and 6. Studying an isotropic film on top of an orthotropic substrate with the constitutive relations obtained in "Appendix 2" is another approach to understand this limit.

6.3 Folding

Our primary focus in this paper was to analyze the impact of fiber on wrinkling. However, Figs. 12 and 13 show a limited FE analysis of post-wrinkling instabilities for fibers oriented in the x-y plane. For $k_1/\mu_s = 2$, the strain required for the wrinkle-to-fold transition increases in the sequence $\theta = 90^{\circ}, 60^{\circ}, 45^{\circ}$, which suggests that this transition can



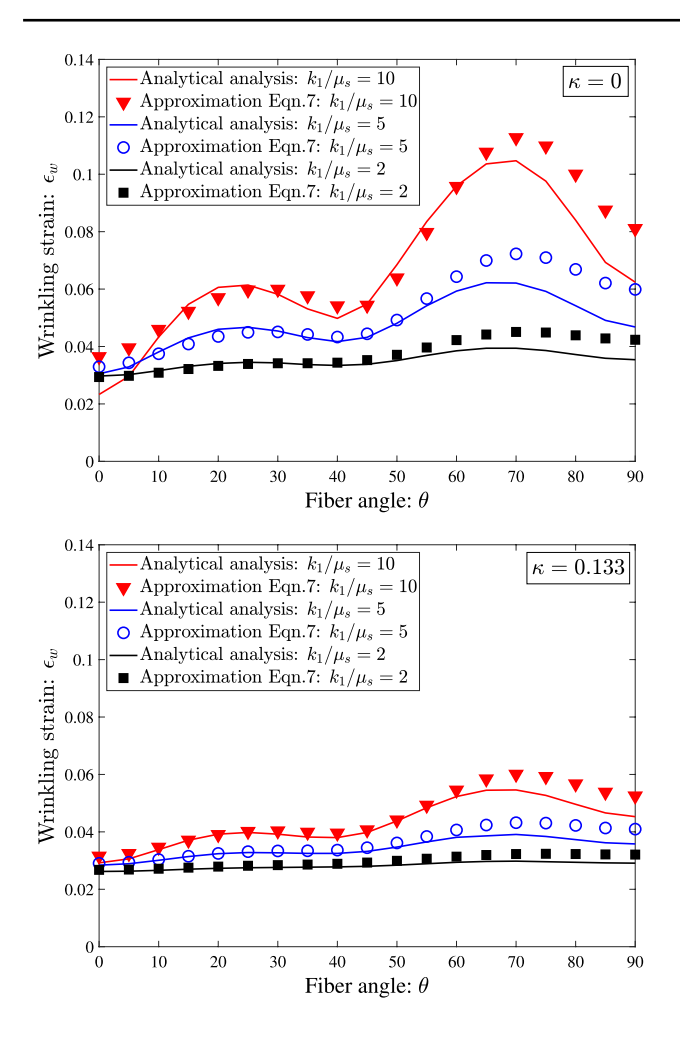
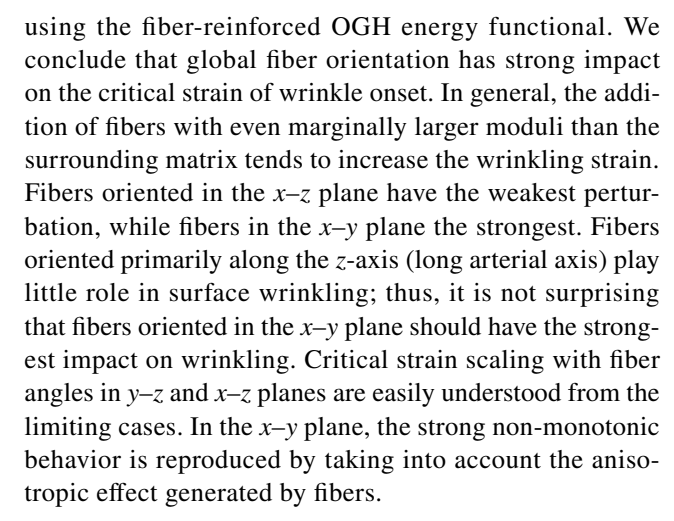


Fig. 14 Approximation based on linearized orthotropic moduli predicts the behavior of $\epsilon_{\rm w}$ for two different κ values in (x-y) fiber plane

either be promoted or inhibited by fiber orientation. Folding occurs once a given wrinkle begins to deviate from the square root law and develops a more linear scaling with ϵ , as predicted in our prior work (Pocivavsek et al. 2008). Future work will focus on a more detailed study of folding on OGH substrates, since folds are also clearly seen in native arteries as demonstrated by our experiments.

7 Conclusion

We show experimentally that native arteries wrinkle and fold as a function of intra-luminal pressure or azimuthal compression, that the wrinkling observed in arteries follows scaling laws derived for stiffness mismatched bilayers, and that arteries also undergo post-wrinkling instabilities such as folds, which again follow scalings expected from the past literature. Furthermore, we perform a detailed computational and analytical analysis of wrinkling in a bilayer system where the substrate is modeled



Acknowledgements L.P. gratefully acknowledges the support of the Department of Surgery, University of Chicago. N.N., E.T., and S.V. acknowledge support from NSF-1824708 and NIH R56-HL142743-01. S.V. acknowledges support from NSF-1561789. N.N. acknowledges funding from NIH-T32 #HL098036. L.D. gratefully acknowledges the partial support of the following grants: (1) PRIN 2017 20177TTP3S and H2020 FET Proactive project NEUROFIBERS, (2) The Italian MIUR with the "Departments of Excellence" Grant L. 232/2016, (3) ARS01-01384-PROSCAN. L.D. also acknowledges the participation to the NIH R56-HL142743-01 grant although without financial support from it. We are grateful to Simon Watkins and the personnel at the Center for Biological Imaging at the University of Pittsburgh for assistance with imaging. This research was supported in part by the University of Pittsburgh Center for Research Computing through the resources provided.

Appendix 1: Perturbation analysis for wrinkling in neo-Hookean/Ogden-Gasser-Holzapfel Bilayer

Summary of notations

Symbols	Notation meaning
\overline{L}	Length of the bilayer
H, h	Substrate and film thicknesses
$\lambda_x = \lambda_1, \lambda_2, \lambda_3$	Applied stretch in x , y , z directions, respectively
δ	Perturbation amplitude
α	Parameter determined in the eigenvalue analysis
λ, k	Wavelength and wave number: $k = \frac{2\pi}{\lambda}$
ϵ	The applied strain: $\epsilon = \frac{\Delta L}{L}$
$\epsilon_{ m w}$	Critical wrinkling strain
k_1, k_2	Fiber stiffness, fiber nonlinearity parameter
κ, θ	Fiber dispersion, orientation
L_i	Unit vector of the direction of the <i>i</i> th fiber family



Symbols	Notation meaning
σ, P, S, N	Cauchy, first and second Piola–Kirchhoff, nominal stresses
F, C, B	Deformation gradient, right and left Cauchy– Green tensor
$I_1, I_{4ii} = L_i^{\mathrm{T}} C L_i$	Invariants of the Cauchy-Green tensor
$\mu_{\mathrm{f}}, \mu_{\mathrm{s}}$	Shear modulus of film and substrate matrix
$u_{\rm f}, v_{\rm f}, u_{\rm s}, v_{\rm s}$	Displacement in the film and substrate

Bifurcation of a thin, stiff neo-Hookean layer on an OGH substrate

A bilayer composed of a thin, stiff incompressible neo-Hookean film attached to a soft, incompressible OGH substrate is subjected to compression as shown in Fig. 15.

Assume that the deformation is plane strain and uniform with the deformation state described in Eq. 8.

$$x = \lambda_x X$$

$$y = \frac{1}{\lambda_x} Y$$
(8)

where (X, Y) are coordinates in the undeformed configuration and (x, y) are the corresponding coordinates in the current configuration. λ_x is the lateral stretch in the x direction.

Consider the perturbation of this homogeneous deformation state with the generic forms of perturbation shown in Eq. 9 for the case of incompressibility (Sun et al. 2012):

$$x = \lambda_x X - \alpha \delta \lambda_x^2 \lambda \sin(kX) e^{\alpha kY}$$

$$y = \frac{1}{\lambda_x} Y + \delta \lambda \cos(kX) e^{\alpha kY}$$

$$p = p_0 + \delta p_1 \cos(kX) e^{\alpha kY}$$
(9)

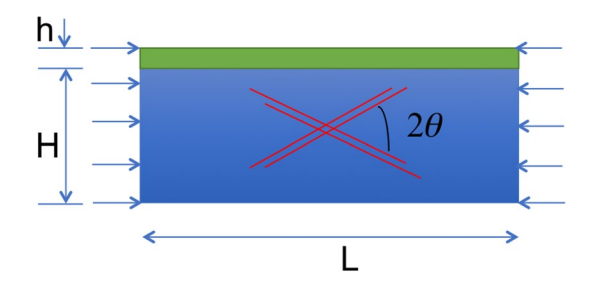


Fig. 15 Thin stiff incompressible neo-Hookean film attached to a soft, incompressible OGH substrate with two symmetric families of fibers

where $\delta << 1$ is the perturbation amplitude parameter. $k=\frac{2\pi}{\lambda}$ is the wrinkle wave number, λ is the undeformed-configurational wavelength of the perturbation. α is a parameter to be determined from the equilibrium condition. p is the hydrostatic pressure for incompressible solids. p_0, p_1 are to be determined from boundary conditions.

The deformation state of each layer in the bilayer due to the above perturbation is a linear combination of each layer 's eigenmodes when each layer is considered separately and is subjected to the same perturbation. Therefore, in the followings, we first will consider the perturbation of each layer individually. A linear combination of the obtained eigenmodes will then be used to construct the deformation state of each layer in the bilayer system. Continuity conditions at the interface between the two layers and boundary conditions at the free surface are used next to construct an eigenvalue problem to determine the critical onset of wrinkling. Finally, the critical wrinkling strain is determined by numerically solving the resulting eigenvalue problem.

Analysis of eigenmodes of the neo-Hookean film

The analysis of eigenmodes of a neo-Hookean layer has been carried out in Sun et al. (2012), Cao and Hutchinson (2012), Stewart et al. (2016). Specifically, consider the neo-Hookean strain energy density function given in Eq. 10:

$$W_{\rm NH} = \mu_{\rm f}(I_1 - 3) \tag{10}$$

First Piola–Kirchhoff stress can be determined from this strain energy function by taking the derivative with respect to the deformation gradients *F* and taking into account the hydrostatic pressure due to incompressibility, specifically:

$$P_{ij} = \frac{\partial W_{\text{NH}}}{\partial F_{ii}} - pF_{ji}^{-1} \tag{11}$$

Note that the deformation gradient can be determined from Eq. (9) for the perturbation state. Specifically,

$$F_{11} = \frac{\partial x}{\partial X} = \lambda_x - \alpha \delta \lambda_x^2 \lambda k \left[\cos(kX) e^{\alpha kY} \right]$$

$$F_{12} = \frac{\partial x}{\partial Y} = -\alpha^2 \delta \lambda_x^2 \lambda k \left[\sin(kX) e^{\alpha kY} \right]$$

$$F_{21} = \frac{\partial y}{\partial X} = -\delta \lambda k \left[\sin(kX) e^{\alpha kY} \right]$$

$$F_{22} = \frac{\partial y}{\partial Y} = \frac{1}{\lambda_x} + \delta \lambda \alpha k \left[\cos(kX) e^{\alpha kY} \right]$$

$$F_{13} = F_{31} = F_{23} = F_{32} = 0, \quad F_{33} = 1$$

$$(12)$$

Note that this prescribed deformation gradient already satisfies the incompressibility constraint $det(F) = 1 + O(\delta^2)$.

The first invariant I_1 is the trace of the left Cauchy–Green tensor $B = F^T F$, which is:



$$B = \begin{bmatrix} F_{11} & F_{12} & 0 \\ F_{21} & F_{22} & 0 \\ 0 & 0 & 1 \end{bmatrix} \begin{bmatrix} F_{11} & F_{21} & 0 \\ F_{12} & F_{22} & 0 \\ 0 & 0 & 1 \end{bmatrix}$$

$$= \begin{bmatrix} F_{11}^{2} + F_{12}^{2} & F_{11}F_{21} + F_{12}F_{22} & 0 \\ F_{21}F_{11} + F_{22}F_{12} & F_{21}^{2} + F_{22}^{2} & 0 \\ 0 & 0 & 1 \end{bmatrix}$$
(13)

and

$$I_1 = \operatorname{trace}(B) = F_{11}^2 + F_{12}^2 + F_{21}^2 + F_{22}^2 + 1 \tag{14}$$

With the consideration of incompressibility det(F) = 1 or $F_{11}F_{22} - F_{12}F_{21} = 1$, the inverse of the deformation gradient F^{-1} becomes:

$$F^{-1} = \frac{1}{F_{11}F_{22} - F_{12}F_{21}} \begin{bmatrix} F_{22} & -F_{12} & 0\\ -F_{21} & F_{11} & 0\\ 0 & 0 & 1 \end{bmatrix}$$

$$= \begin{bmatrix} F_{22} & -F_{12} & 0\\ -F_{21} & F_{11} & 0\\ 0 & 0 & 1 \end{bmatrix}$$
(15)

Hence,

$$P_{11} = \frac{\partial W_{\text{NH}}}{\partial F_{11}} - pF_{11}^{-1} = \mu_{\text{f}} \frac{\partial I_{1}}{\partial F_{11}} - pF_{11}^{-1}$$

$$= 2\mu_{\text{f}} F_{11} - \left[p_{0} + \delta p_{1} \cos(kX) e^{\alpha kY} \right] F_{22}$$

$$P_{12} = \frac{\partial W_{\text{NH}}}{\partial F_{12}} - pF_{21}^{-1} = \mu_{\text{f}} \frac{\partial I_{1}}{\partial F_{12}} - pF_{21}^{-1}$$

$$= 2\mu_{\text{f}} F_{12} + \left[p_{0} + \delta p_{1} \cos(kX) e^{\alpha kY} \right] F_{21}$$

$$P_{21} = \frac{\partial W_{\text{NH}}}{\partial F_{21}} - pF_{12}^{-1} = \mu_{\text{f}} \frac{\partial I_{1}}{\partial F_{21}} - pF_{12}^{-1}$$

$$= 2\mu_{\text{f}} F_{21} + \left[p_{0} + \delta p_{1} \cos(kX) e^{\alpha kY} \right] F_{12}$$

$$P_{22} = \frac{\partial W_{\text{NH}}}{\partial F_{22}} - pF_{22}^{-1} = \mu_{\text{f}} \frac{\partial I_{1}}{\partial F_{22}} - pF_{22}^{-1}$$

$$= 2\mu_{\text{f}} F_{22} - \left[p_{0} + \delta p_{1} \cos(kX) e^{\alpha kY} \right] F_{11}$$

$$(16)$$

Note that for a more compact form, Eq. 16 can be written in the matrix form which can be easily derived from the second Piola Kirchhoff stress $S = 2 \frac{\partial W_{\text{NH}}}{\partial C}$. Specifically,

$$S = 2\mu_{\rm f} \frac{\partial I_1}{\partial C} = 2\mu_{\rm f} I$$

$$P = FS - pF^{-T} = 2\mu_{\rm f} F - pF^{-T}$$
(17)

which are consistent with the stresses using index notations in Eq. 16.

Substituting Eq. 12 into Eq. 16, the calculations result in the following formulae for first Piola–Kirchhoff stress:

$$P_{11} = \left(2\mu_{\rm f}\lambda_x - p_0 \frac{1}{\lambda_x}\right)$$

$$-\delta \left\{2\mu_{\rm f}k\alpha\lambda_x^2\lambda + p_0k\alpha\lambda + \frac{p_1}{\lambda_x}\right\} \cos(kX)e^{\alpha kY}$$

$$+ O(\delta^2)$$

$$P_{12} = -\delta \left(2\mu_{\rm f}k\alpha^2\lambda_x^2\lambda + p_0k\lambda\right) \sin(kX)e^{\alpha kY} + O(\delta^2)$$

$$P_{21} = -\delta \left(2\mu_{\rm f}k\lambda + p_0k\alpha^2\lambda_x^2\lambda\right) \sin(kX)e^{\alpha kY} + O(\delta^2)$$

$$P_{22} = \left(\frac{2\mu_{\rm f}}{\lambda_x} - p_0\lambda_x\right)$$

$$+ \delta \left(2\mu_{\rm f}k\alpha\lambda + p_0k\alpha\lambda_x^2\lambda - \lambda_x p_1\right) \cos(kX)e^{\alpha kY}$$

$$+ O(\delta^2)$$
(18)

The zeroth order $(\delta=0)$ solution is obtained from Eq. 18, and from the boundary condition for the single layer $P_{22}^0=0$, it is shown that $p_0=\frac{2\mu_{\rm f}}{\lambda_{\rm r}^2}$

Substituting the stresses into the two following equilibrium equations, the following 2 equations are obtained:

$$P_{11,X} + P_{12,Y} = \left\{ 4\pi \mu_{f} \alpha \lambda_{x}^{2} \left(1 - \alpha^{2} \right) + \frac{p_{1}}{\lambda_{x}} \right\}$$

$$\delta k \sin(kX) e^{\alpha kY} + O(\delta^{2}) = 0$$

$$P_{12,X} + P_{22,Y} = \left(-4\pi \mu_{f} + 4\pi \mu_{f} \alpha^{2} - \lambda_{x} \alpha p_{1} \right)$$

$$\delta k \cos(kX) e^{\alpha kY} + O(\delta^{2}) = 0$$
(19)

which leads to:

$$4\pi\mu_{\rm f}\alpha\lambda_x^2(1-\alpha^2) + \frac{p_1}{\lambda_x} = 0$$

$$-4\pi\mu_{\rm f} + 4\pi\mu_{\rm f}\alpha^2 - \lambda_x\alpha p_1 = 0$$
(20)

From the first part of Eq. 20, $p_1 = -4\pi \mu_f \alpha \lambda_x^3 (1 - \alpha^2)$. Substituting this p_1 into the second part of Eq. 20 yields a fourth-order equation of α : $4\pi \mu_f (\lambda_x^4 \alpha^2 - 1)(1 - \alpha^2) = 0$. Solving this equation gives four solutions of α and hence 4 pairs of solutions (α_i, p_i) corresponding with 4 eigenvalues: $\alpha = 1, \alpha = -1, \alpha = 1/\lambda_x^2, \alpha = -1/\lambda_x^2$. Substituting each pair of solutions into Eqs. (9) and (18) provides an eigenmode and its stress state for the single neo-Hookean layer subjected to perturbation. Specifically, from Eq. (9), $(u_{fi}, v_{fi}), i = \overline{1, 4}$ are obtained for the deformation where $u = x - \lambda_x X, v = y - Y/\lambda_x$. From Eq. (18), tangential and normal tractions $N_{fi_{21}}, N_{fi_{22}}, i = \overline{1, 4}$ are obtained from the nominal stresses, respectively. Nominal stress is determined as $N = P^T$.

Analysis of eigenmodes of the OGH substrate

Consider the OGH substrate with the strain energy density function given in Eq. 21.



$$W_{\text{OGH}} = \mu_{\text{s}}(I_1 - 3) + \frac{k_1}{2k_2} \sum_{m=1}^{N} \left\{ \exp\left[k_2 E_{\text{m}}^2\right] - 1 \right\}$$

$$E_{\text{m}} = \kappa(I_1 - 3) + (1 - 3\kappa)(I_{4\text{mm}} - 1)$$
(21)

where the invariant $I_{4\text{mm}} = L_{\text{m}} \cdot (CL_{\text{m}})$, L_{m} is the unit direction of the fiber family m th, $C = F^{\text{T}}F$ is the right Cauchy Green tensor.

With the same approach as in Sect. 1.1, the first Piola–Kirchhoff stress can be determined by taking the derivative of the energy with respect to the deformation gradient.

$$P_{ij} = \frac{\partial W_{\text{OGH}}}{\partial F_{ii}} - pF_{ji}^{-1} \tag{22}$$

or from the second Piola–Kirchhoff stress *S*:

$$P = FS - pF^{-T} = 2F \frac{\partial W_{\text{OGH}}}{\partial C} - pF^{-T}$$
 (23)

where the second Piola-Kirchhoff stress is:

$$S = 2\frac{\partial W_{\text{OGH}}}{\partial C} = 2\mu_{\text{s}} \frac{\partial I_{1}}{\partial C} + \frac{k_{1}}{k_{2}} \sum_{m=1}^{2} \left\{ 2k_{2}E_{\text{m}} \exp\left[k_{2}E_{\text{m}}^{2}\right] \frac{\partial E_{i}}{\partial C} \right\}$$

$$S = 2\mu_{\text{s}}I + 2k_{1} \sum_{m=1}^{2} E_{\text{m}} \exp\left[k_{2}E_{\text{m}}^{2}\right] \left\{ \kappa \frac{\partial I_{1}}{\partial C} + (1 - 3\kappa) \frac{\partial I_{4mm}}{\partial C} \right\}$$

$$S = 2\mu_{\text{s}}I + \sum_{m=1}^{2} 2k_{1}\kappa E_{\text{m}} \exp\left[k_{2}E_{\text{m}}^{2}\right]I + \sum_{m=1}^{2} 2k_{1}(1 - 3\kappa)E_{\text{m}} \exp\left[k_{2}E_{\text{m}}^{2}\right]L_{\text{m}} \otimes L_{\text{m}}$$

$$(24)$$

Thus, the first Piola-Kirchhoff stress becomes:

$$P = -PF^{-T} + 2\mu_{s}F + \sum_{m=1}^{2} 2k_{1}\kappa E_{m} \exp\left[k_{2}E_{m}^{2}\right]F$$

$$+ \sum_{m=1}^{2} 2k_{1}(1 - 3\kappa)E_{m} \exp\left[k_{2}E_{m}^{2}\right]F\left(L_{m} \otimes L_{m}\right)$$
(25)

With the given deformation gradient in Eq. (9), components of the first Piola–Kirchhoff stress corresponding to the OGH layer are specified in Eq. 25. Hence, from the zeroth-order solution with the boundary condition $P_{22}^0 = 0$, p_0 is determined.

Substituting these stresses into the two equilibrium equations (in Eq. 19) and applying the same solution

method as in Sect. 1.1, a fourth-order equation in terms of α is again obtained. Hence, 4 pairs of solutions (α_i, p_i) are determined. However, for the substrate, as the undulation dies down as $Y \to -\infty$, only 2 solutions with positive values of α are used to construct eigenmodes for the substrate. Specifically, from Eq. (9), (u_{si}, v_{si}) , $i = \overline{1,2}$ are obtained for the deformation where $u = x - \lambda_x X$, $v = y - Y/\lambda_x$. From Eq. (25), tangential and normal tractions $N_{si_{21}}, N_{si_{22}}, i = \overline{1,2}$ are obtained from the nominal stresses, respectively. Nominal stress is determined as $N = P^T$.

Note that for a neo-Hookean layer, the 4 eigenvalues α are all real values. However, solving the fourth-order equation of eigenvalues α for the OGH substrate can result in complex solutions. If the eigenvalues α for the OGH substrate are complex, the four eigenvalues will correspond to two pairs of complex conjugate. As the undulation must vanish when $Y \to -\infty$, the pair of complex conjugate with the positive real part is chosen for constructing the eigenmodes for the substrate. Actually, as this is a pair of conjugate eigenvalues α , only one is needed. With this eigenvalue, it is straightforward to compute (u_{si}, v_{si}) and $N_{si_{21}}, N_{si_{22}}$ which are the corresponding deformation and stresses. As α is a complex value, these deformation and stress fields are also complex. The real parts and the complex parts of the fields are used now to construct the 2 eigenmodes of the OGH substrate.

Due to the cumbersome formulae, all the calculations for the stresses, equilibrium equations, and eigenvalue problems are implemented in Matlab.

Linear combination of eigenmodes for the bilayer system

Recall: (u_{fi}, v_{fi}) , $i = \overline{1,4}$ and $N_{fi_{21}}, N_{fi_{22}}$, $i = \overline{1,4}$ as the deformation and stresses, respectively, associated with 4 eigenmodes of the neo-Hookean layer. (u_{si}, v_{si}) , $i = \overline{1,2}$ and $N_{si_{21}}, N_{si_{22}}, i = \overline{1,2}$ as the deformation and nominal stresses, respectively, associated with 2 eigenmodes of the OGH layer.

For a bilayer composed of a neo-Hookean film attached to an OGH substrate subjected to the perturbation in Eq. 9, the deformation in each layer is a linear combination of its eigenmodes. In other words, the deformation in the neo-Hookean film can be written as:

$$u_{f} = A_{1}u_{f1} + A_{2}u_{f2} + A_{3}u_{f3} + A_{4}u_{f4}$$

$$v_{f} = A_{1}v_{f1} + A_{2}v_{f2} + A_{3}v_{f3} + A_{4}v_{f4}$$

$$N_{f_{21}} = A_{1}N_{f1_{21}} + A_{2}N_{f2_{21}} + A_{3}N_{f3_{21}} + A_{4}N_{f4_{21}}$$

$$N_{f_{22}} = A_{1}N_{f1_{22}} + A_{2}N_{f2_{22}} + A_{3}N_{f3_{22}} + A_{4}N_{f4_{22}}$$
(26)

The deformation in the OGH substrate can be written as:



$$u_{s} = A_{5}u_{s1} + A_{6}u_{s2}$$

$$v_{s} = A_{5}v_{s1} + A_{6}v_{s2}$$

$$N_{s_{21}} = A_{5}N_{s1_{21}} + A_{6}N_{s2_{21}}$$

$$N_{s_{22}} = A_{5}N_{s1_{22}} + A_{6}N_{s2_{22}}$$
(27)

where $A_1, A_2, A_3, A_4, A_5, A_6$ are constant parameters.

Continuity and boundary conditions—eigenvalue problem for critical strain

At the interface between the film and the substrate, Y = 0, continuity in displacements and tractions are enforced which can be written as follows:

$$u_{f}(Y=0) = u_{s}(Y=0)$$

$$v_{f}(Y=0) = v_{s}(Y=0)$$

$$N_{f_{21}}(Y=0) = N_{s_{21}}(Y=0)$$

$$N_{f_{22}}(Y=0) = N_{s_{22}}(Y=0)$$
(28)

At the stress-free face Y = h of the neo-Hookean film, two boundary conditions for tractions are obtained:

$$N_{f_{21}}(Y = h) = 0$$

 $N_{f_{22}}(Y = h) = 0$ (29)

Critical wrinkling strain determination

By substituting the linear combinations in Eqs. 26, 27 into the system of continuity and boundary conditions in Eqs. 28 and 29, a system of the following forms is obtained:

$$F(\lambda_{x}, kh) \begin{bmatrix} A_{1} \\ A_{2} \\ A_{3} \\ A_{4} \\ A_{5} \\ A_{6} \end{bmatrix} = 0$$
(30)

The critical wrinkling strain, which is minimized over all kh is determined from the nonlinear equations det(F) = 0. This is solved numerically in Matlab.

Appendix 2: Linearization of OGH model for material properties

Figure 16 plots the prediction of $\frac{(kh)^2}{\epsilon_w}$ ratio for bilayers of a neo-Hookean film bonded to an OGH substrate.

When the fiber stiffness $k_1 = 0$, the substrate becomes neo-Hookean. The ratio approaches the value of 4 for $\mu_f >> \mu_s$, which is demonstrated in Fig. 16 for the

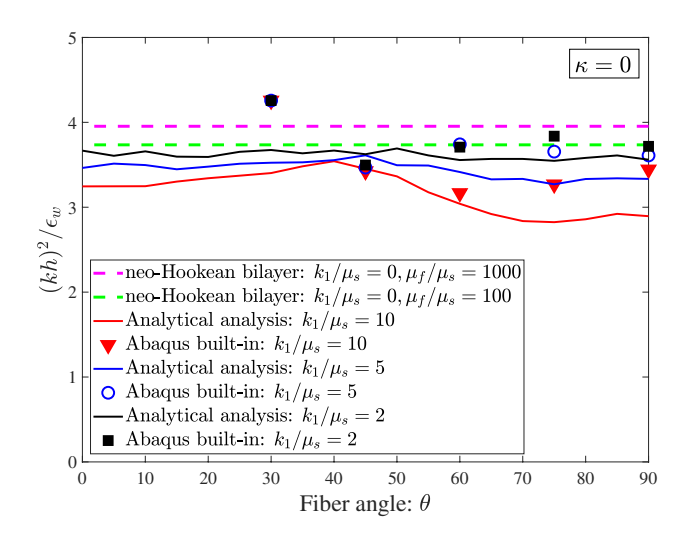


Fig. 16 Ratio $\frac{(kh)^2}{\epsilon_w}$ versus fiber angle θ for the case of fiber dispersion $\kappa = 0$ in (x-y) fiber plane

mismatch modulus ratio $\mu_{\rm f}/\mu_{\rm s}=1000$. At lower mismatch ratio, the value of $\frac{(kh)^2}{\epsilon_w}$ is slightly less than 4. Specifically, with a mismatch modulus ratio μ_f/μ_s of 100 as considered in this paper, $\frac{(kh)^2}{\epsilon_w} \sim 3.7$. When fiber stiffness is nonzero, the renormalization of the substrate stiffness must change the effective value of the substrate stiffness and lead to deviations of this ratio from the constant value. At low fiber stiffness $k_1/\mu_s = 2$, $k_1/\mu_s = 5$, the ratio remains constant around the value of the corresponding neo-Hookean bilayer with the same modulus mismatch $\mu_f/\mu_s = 100$. For higher fiber stiffness $k_1/\mu_s = 10$, the ratio shows some deviations from this constant trend, especially at high values of fiber angle θ . Note that as angle θ increases, the transverse direction y also has higher stiffness. The deviation, therefore, might be attributed to the effect of orthotropic material properties associated with OGH model which become more significant as fibers are stiffer and oriented in the transverse (y) direction. These properties are derived through linearization as follows.

Ogden-Gasser-Holzapfel substrate with strain energy density function:

$$W_{\text{OGH}} = \mu(I_1 - 3) + \frac{k_1}{2k_2} \sum_{i=1}^{N} \left\{ \exp\left[k_2 E_i^2\right] - 1 \right\}$$

$$E_i = \kappa(I_1 - 3) + (1 - 3\kappa)(I_{4ii} - 1)$$

$$I_{4ii} = L_i^{\text{T}} C L_i$$
(31)

where $C = F^{T}F$ is the right Cauchy–Green tensor, F is the deformation gradient, L_i is the unit vector of the orientation of the *i*th fiber family. Here, N = 2 corresponds to two fiber families.



The second Piola-Kirchhoff stress:

$$S = 2\frac{\partial W_{\text{OGH}}}{\partial C}$$

$$= 2\mu \frac{\partial I_1}{\partial C} + \frac{k_1}{k_2} \sum_{i=1}^{2} \left\{ 2k_2 E_i \exp\left[k_2 E_i^2\right] \frac{\partial E_i}{\partial C} \right\}$$

$$S = 2\mu I + 2k_1 \sum_{i=1}^{2} E_i \exp\left[k_2 E_i^2\right]$$

$$\left\{ \kappa \frac{\partial I_1}{\partial C} + (1 - 3\kappa) \frac{\partial I_{4i}}{\partial C} \right\}$$
(32)

$$\begin{split} S &= 2\mu I + \sum_{i=1}^{2} 2k_{1}\kappa E_{i} \text{exp}\big[k_{2}E_{i}^{2}\big]I \\ &+ \sum_{i=1}^{2} 2k_{1}(1-3\kappa)E_{i} \text{exp}\big[k_{2}E_{i}^{2}\big]L_{i} \otimes L_{i} \end{split}$$

Cauchy stress for incompressible case:

$$\sigma = FSF^{T} = -pI + 2\mu B + \sum_{i=1}^{2} 2k_{1}\kappa E_{i} \exp\left[k_{2}E_{i}^{2}\right]B$$

$$+ \sum_{i=1}^{2} 2k_{1}(1 - 3\kappa)E_{i} \exp\left[k_{2}E_{i}^{2}\right]FL_{i} \otimes FL_{i}$$
(33)

where $B = FF^{T}$ is the left Cauchy Green tensor.

For two family fibers lying in x-y plane: $L_1 = [c, s, 0]^T$, $L_2 = [c, -s, 0]^T$, $c = \cos(\theta)$, $s = \sin(\theta)$ where θ is the fiber angle with respect to x-axis.

Determine longitudinal moduli and Poisson's ratios

Consider a block made of OGH material being subjected to tension in one direction and free to expand in the other two directions. The deformation gradient F, left Cauchy–Green tensor B, right Cauchy–Green tensor C are described as follows:

$$F = \begin{bmatrix} \lambda_1 & 0 & 0 \\ 0 & \lambda_2 & 0 \\ 0 & 0 & \lambda_3 \end{bmatrix}, \quad B = C = \begin{bmatrix} \lambda_1^2 & 0 & 0 \\ 0 & \lambda_2^2 & 0 \\ 0 & 0 & \lambda_3^2 \end{bmatrix}$$
(34)

where the three stretch ratios are related by incompressibility restriction: $\lambda_1 \lambda_2 \lambda_3 = 1$. Other quantities in Eq. (33) for computing Cauchy stresses become:

$$FL_{1} = \begin{bmatrix} \lambda_{1} & 0 & 0 \\ 0 & \lambda_{2} & 0 \\ 0 & 0 & \lambda_{3} \end{bmatrix} \begin{bmatrix} c \\ s \\ 0 \end{bmatrix} = \begin{bmatrix} c\lambda_{1} \\ s\lambda_{2} \\ 0 \end{bmatrix},$$

$$FL_{2} = \begin{bmatrix} \lambda_{1} & 0 & 0 \\ 0 & \lambda_{2} & 0 \\ 0 & 0 & \lambda_{3} \end{bmatrix} \begin{bmatrix} c \\ -s \\ 0 \end{bmatrix} = \begin{bmatrix} c\lambda_{1} \\ -s\lambda_{2} \\ 0 \end{bmatrix}$$
(35)

$$I_{41} = \begin{bmatrix} c & s & 0 \end{bmatrix} \begin{bmatrix} \lambda_1^2 & 0 & 0 \\ 0 & \lambda_2^2 & 0 \\ 0 & 0 & \lambda_3^2 \end{bmatrix} \begin{bmatrix} c \\ s \\ 0 \end{bmatrix}$$
$$= c^2 \lambda_1^2 + s^2 \lambda_2^2$$
(36)

$$I_{42} = \begin{bmatrix} c & -s & 0 \end{bmatrix} \begin{bmatrix} \lambda_1^2 & 0 & 0 \\ 0 & \lambda_2^2 & 0 \\ 0 & 0 & \lambda_3^2 \end{bmatrix} \begin{bmatrix} c \\ -s \\ 0 \end{bmatrix}$$
$$= c^2 \lambda_1^2 + s^2 \lambda_2^2$$
(37)

$$E_1 = E_2 = \kappa (I_1 - 3) + (1 - 3\kappa)(c^2 \lambda_1^2 + s^2 \lambda_2^2 - 1)$$
(38)

$$FL_{1} \otimes FL_{1} = \begin{bmatrix} c\lambda_{1} \\ s\lambda_{2} \\ 0 \end{bmatrix} \begin{bmatrix} c\lambda_{1} & s\lambda_{2} & 0 \end{bmatrix}$$

$$= \begin{bmatrix} c^{2}\lambda_{1}^{2} & cs\lambda_{1}\lambda_{2} & 0 \\ cs\lambda_{1}\lambda_{2} & s^{2}\lambda_{2}^{2} & 0 \\ 0 & 0 & 0 \end{bmatrix}$$
(39)

$$FL_{2} \otimes FL_{2} = \begin{bmatrix} c\lambda_{1} \\ -s\lambda_{2} \\ 0 \end{bmatrix} \begin{bmatrix} c\lambda_{1} & -s\lambda_{2} & 0 \end{bmatrix}$$

$$= \begin{bmatrix} c^{2}\lambda_{1}^{2} & -cs\lambda_{1}\lambda_{2} & 0 \\ -cs\lambda_{1}\lambda_{2} & s^{2}\lambda_{2}^{2} & 0 \\ 0 & 0 & 0 \end{bmatrix}$$
(40)

Substituting Eqs. (34–40) into Eq. (33), three components of Cauchy stresses for the block being pulled in one direction:

$$\sigma_{11} = -p + 2\mu\lambda_1^2 + 4\kappa k_1 E_1 \exp\left[k_2 E_1^2\right] \lambda_1^2 + 4(1 - 3\kappa)k_1 E_1 \exp\left[k_2 E_1^2\right] c^2 \lambda_1^2 \sigma_{22} = -p + 2\mu\lambda_2^2 + 4\kappa k_1 E_1 \exp\left[k_2 E_1^2\right] \lambda_2^2 + 4(1 - 3\kappa)k_1 E_1 \exp\left[k_2 E_1^2\right] s^2 \lambda_2^2 \sigma_{33} = -p + 2\mu\lambda_3^2 + 4\kappa k_1 E_1 \exp\left[k_2 E_1^2\right] \lambda_3^2$$

$$(41)$$

Stretching along the x direction to determine E_x , v_{xy} , v_{xz}

Note that the block is pulled in *x* direction and is free to expand in *y* and *z* directions, therefore:

$$\sigma_{11} \neq 0, \sigma_{22} = 0, \sigma_{33} = 0 \tag{42}$$

thus, using $\lambda_3 = \frac{1}{\lambda_1 \lambda_2}$, they can be written:



$$\begin{split} \sigma_{11} &= \sigma_{11} - \sigma_{33} = 2\mu \left\{ \lambda_1^2 - \frac{1}{\lambda_1^2 \lambda_2^2} \right\} \\ &+ 4\kappa k_1 E_1 \exp[k_2 E_1^2] \left[\lambda_1^2 - \frac{1}{\lambda_1^2 \lambda_2^2} \right] \\ &+ 4(1 - 3\kappa) k_1 E_1 \exp[k_2 E_1^2] c^2 \lambda_1^2 \\ \sigma_{22} &= \sigma_{22} - \sigma_{33} = 2\mu \left\{ \lambda_2^2 - \frac{1}{\lambda_1^2 \lambda_2^2} \right\} \\ &+ 4\kappa k_1 E_1 \exp[k_2 E_1^2] \left[\lambda_2^2 - \frac{1}{\lambda_1^2 \lambda_2^2} \right] \\ &+ 4(1 - 3\kappa) k_1 E_1 \exp[k_2 E_1^2] s^2 \lambda_2^2 \end{split}$$

$$(43)$$

Consider small deformation regime, the strains are small and their high order terms can be neglected. Thus, the following approximations can be used to approximate the stresses:

$$\begin{split} \lambda_1 &= 1 + \epsilon_1, \, \lambda_2 = 1 + \epsilon_2, \, \lambda_1^2 = 1 + 2\epsilon_1, \, \lambda_2^2 = 1 + 2\epsilon_2 \\ \frac{1}{\lambda_1^2} &= 1 - 2\epsilon_1, \, \frac{1}{\lambda_2^2} = 1 - 2\epsilon_2, \, \frac{1}{\lambda_1^2 \lambda_2^2} = 1 - 2\epsilon_1 - 2\epsilon_2 \\ I_1 &= \lambda_1^2 + \lambda_2^2 + \lambda_3^2 = 3 \\ I_{41} &= I_{42} = c^2 \lambda_1^2 + s^2 \lambda_2^2 = 1 + 2c^2 \epsilon_1 + 2s^2 \epsilon_2 \\ E_1 &= E_2 = (1 - 3\kappa) \left(2c^2 \epsilon_1 + 2s^2 \epsilon_2 \right) \\ \exp \left[k_2 E_1^2 \right] &= 1 \end{split}$$

$$(44)$$

Substituting the approximations in Eq. (44) into Eq. (43), the stresses become:

$$\sigma_{11} = 2\mu(4\epsilon_1 + 2\epsilon_2) + 8k_1(1 - 3\kappa)^2(c^4\epsilon_1 + c^2s^2\epsilon_2)$$

$$\sigma_{22} = 2\mu(4\epsilon_2 + 2\epsilon_1) + 8k_1(1 - 3\kappa)^2(c^2s^2\epsilon_1 + s^4\epsilon_2)$$
(45)

since $\sigma_{22} = 0$, so we have:

$$\frac{\epsilon_2}{\epsilon_1} = -v_{xy} = -\frac{4\mu + 8k_1(1 - 3\kappa)^2 c^2 s^2}{8\mu + 8k_1(1 - 3\kappa)^2 s^4}$$
(46)

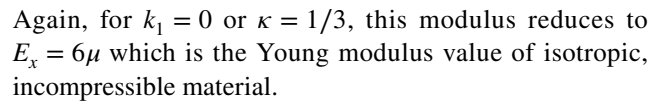
Note that we are pulling in the x direction, so this ratio between the two strains gives the Poisson's ratio v_{xy} . It can be seen that for the case of isotropic material, i.e., $k_1 = 0$ or $\kappa = 1/3$, this ratio is equal to 0.5 which is the Poisson's ratio of isotropic incompressible material.

By substituting ϵ_2 in terms of ϵ_1 into σ_{11} , we have:

$$\sigma_{11} = \frac{6\mu^2 + 8k_1\mu(1 - 3\kappa)^2(1 - 3c^2s^2)}{\mu + k_1(1 - 3\kappa)^2s^4}\epsilon_1 \tag{47}$$

The longitudinal modulus in the *x*-direction, thus, can be obtained:

$$E_x = \frac{\sigma_{11}}{\epsilon_{11}} = \frac{6\mu^2 + 8k_1\mu(1 - 3\kappa)^2(1 - 3c^2s^2)}{\mu + k_1(1 - 3\kappa)^2s^4}$$
(48)



Note that:

$$\lambda_3 = \frac{1}{\lambda_1 \lambda_2} = \frac{1}{(1 + \epsilon_1)(1 + \epsilon_2)} = 1 - \epsilon_1 - \epsilon_2 = 1 + \epsilon_3$$

$$\epsilon_1 + \epsilon_2 = -\epsilon_3 \implies 1 + \frac{\epsilon_2}{\epsilon_1} = -\frac{\epsilon_3}{\epsilon_1}$$

$$\Rightarrow v_{xz} = -\frac{\epsilon_3}{\epsilon_1} = \frac{4\mu + 8k_1(1 - 3\kappa)^2 s^2 (s^2 - c^2)}{8\mu + 8k_1(1 - 3\kappa)^2 s^4}$$
(49)

Stretching along the y direction to determine E_y , v_{yx} , v_{yz}

With the same approach, the modulus E_y in y-direction and Poisson's ratio v_{yx} can be derived by subjecting the block to the tension in y-direction. Specifically,

$$\sigma_{11} = 0, \sigma_{22} \neq 0, \sigma_{33} = 0 \tag{50}$$

Thus:

$$\sigma_{11} = \sigma_{11} - \sigma_{33} = \left\{ 8\mu + 8k_1(1 - 3\kappa)^2 c^4 \right\} \epsilon_1 + \left\{ 4\mu + 8k_1(1 - 3\kappa)^2 c^2 s^2 \right\} \epsilon_2 = 0 \sigma_{22} = \sigma_{22} - \sigma_{33} = \left\{ 4\mu + 8k_1(1 - 3\kappa)^2 c^2 s^2 \right\} \epsilon_1 + \left\{ 8\mu + 8k_1(1 - 3\kappa)^2 s^4 \right\} \epsilon_2$$
(51)

The Poisson's ratio v_{vx} is therefore.

$$\frac{\epsilon_1}{\epsilon_2} = -v_{yx} = -\frac{4\mu + 8k_1(1 - 3\kappa)^2 c^2 s^2}{8\mu + 8k_1(1 - 3\kappa)^2 c^4}$$
 (52)

And the modulus E_v :

$$E_{y} = \frac{\sigma_{22}}{\epsilon_{22}} = -\frac{(4\mu + 8k_{1}(1 - 3\kappa)^{2}c^{2}s^{2})^{2}}{8\mu + 8k_{1}(1 - 3\kappa)^{2}c^{4}} + (8\mu + 8k_{1}(1 - 3\kappa)^{2}s^{4})$$

$$E_{y} = \frac{6\mu^{2} + 8k_{1}\mu(1 - 3\kappa)^{2}(1 - 3c^{2}s^{2})}{\mu + k_{1}(1 - 3\kappa)^{2}c^{4}}$$
(53)

The Poisson's ratio v_{yz} is:

$$\epsilon_1 + \epsilon_2 = -\epsilon_3 \implies 1 + \frac{\epsilon_1}{\epsilon_2} = -\frac{\epsilon_3}{\epsilon_2}$$

$$\implies v_{yz} = -\frac{\epsilon_3}{\epsilon_2} = \frac{4\mu + 8k_1(1 - 3\kappa)^2 c^2 (c^2 - s^2)}{8\mu + 8k_1(1 - 3\kappa)^2 c^4}$$
(54)

Pulling in the z direction to determine E_z , v_{zx} , v_{zy}

When the block is subjected to tension in z direction and is free to expand in x, y directions, the stress state becomes:



$$\sigma_{11} = 0, \sigma_{22} = 0, \sigma_{33} \neq 0$$

Using $\sigma_{11} = 0, \sigma_{22} = 0, \sigma_{33} \neq 0$

Using $\lambda_2 = \frac{1}{\lambda_1 \lambda_2}$, Eq. (33) becomes:

$$\begin{split} \sigma_{11} &= -p + 2\mu\lambda_1^2 + 4\kappa k_1 E_1 \exp[k_2 E_1^2]\lambda_1^2 \\ &+ 4(1 - 3\kappa)k_1 E_1 \exp[k_2 E_1^2]c^2\lambda_1^2 = 0 \\ \sigma_{22} &= -p + 2\mu\frac{1}{\lambda_1^2\lambda_3^2} + 4\kappa k_1 E_1 \exp[k_2 E_1^2]\frac{1}{\lambda_1^2\lambda_3^2} \\ &+ 4(1 - 3\kappa)k_1 E_1 \exp[k_2 E_1^2]\frac{s^2}{\lambda_1^2\lambda_2^2} = 0 \end{split}$$

$$\sigma_{33} = -p + 2\mu\lambda_3^2 + 4\kappa k_1 E_1 \exp[k_2 E_1^2]\lambda_3^2$$

$$\begin{split} \sigma_{33} &= \sigma_{33} - \sigma_{22} = 2\mu \left[\lambda_3^2 - \frac{1}{\lambda_1^2 \lambda_3^2} \right] \\ &+ 4\kappa k_1 E_1 \exp[k_2 E_1^2 \left[\lambda_3^2 - \frac{1}{\lambda_1^2 \lambda_3^2} \right] \\ &- 4k_1 E_1 (1 - 3\kappa) \exp[k_2 E_1^2] \frac{s^2}{\lambda_1^2 \lambda_3^2} \\ \sigma_{11} &= \sigma_{11} - \sigma_{22} = 2\mu \left[\lambda_1^2 - \frac{1}{\lambda_1^2 \lambda_3^2} \right] \\ &+ 4\kappa k_1 E_1 \exp[k_2 E_1^2 \left[\lambda_1^2 - \frac{1}{\lambda_1^2 \lambda_3^2} \right] \\ &+ 4k_1 E_1 (1 - 3\kappa) \exp[k_2 E_1^2] \left[c^2 \lambda_1^2 - \frac{s^2}{\lambda_1^2 \lambda_3^2} \right] \end{split}$$

Using small deformation approximations:

$$\begin{split} \lambda_1 &= 1 + \epsilon_1, \lambda_1^2 = 1 + 2\epsilon_1, \frac{1}{\lambda_1^2} = 1 - 2\epsilon_1 \\ \lambda_3 &= 1 + \epsilon_3, \lambda_3^2 = 1 + 2\epsilon_3, \frac{1}{\lambda_3^2} = 1 - 2\epsilon_3 \\ \frac{1}{\lambda_1^2 \lambda_3^2} &= 1 - 2\epsilon_1 - 2\epsilon_3, \lambda_1^2 - \frac{1}{\lambda_1^2 \lambda_3^2} \\ &= 4\epsilon_1 + 2\epsilon_3, \lambda_3^2 - \frac{1}{\lambda_1^2 \lambda_3^2} = 2\epsilon_1 + 4\epsilon_3 \\ \frac{s^2}{\lambda_1^2 \lambda_3^2} &= s^2 (1 - 2\epsilon_1 - 2\epsilon_3) \\ c^2 \lambda_1^2 - \frac{s^2}{\lambda_1^2 \lambda_3^2} &= c^2 - s^2 + 2\epsilon_1 + 2s^2 \epsilon_3 \\ E_1 &= (1 - 3\kappa)(c^2 \lambda_1^2 + \frac{s^2}{\lambda_1^2 \lambda_3^2} - 1) \\ &= (1 - 3\kappa) \left[2(c^2 - s^2)\epsilon_1 - 2s^2 \epsilon_3 \right] \end{split}$$

Substituting Eq. (58) into Eq. (57):

(55)
$$\sigma_{33} = 2\mu(4\epsilon_3 + 2\epsilon_1) - 4k_1(1 - 3\kappa)^2 s^2$$

$$\left[2(c^2 - s^2)\epsilon_1 - 2s^2\epsilon_3\right]$$

$$\sigma_{11} = 2\mu(4\epsilon_1 + 2\epsilon_3) + 4k_1(1 - 3\kappa)^2(c^2 - s^2)$$

$$\left[2(c^2 - s^2)\epsilon_1 - 2s^2\epsilon_3\right] = 0$$
(59)

Therefore, the Poisson's ratio v_{zx} is:

(56)
$$\frac{\epsilon_1}{\epsilon_3} = -v_{zx} = -\frac{4\mu - 8k_1(1 - 3\kappa)^2(c^2s^2 - s^4)}{8\mu + 8k_1(1 - 3\kappa)^2(c^2 - s^2)^2}$$
 (60)

The modulus E_{τ} is:

$$E_z = \frac{6\mu^2 + 8\mu k_1 (1 - 3\kappa)^2 (1 - 3c^2 s^2)}{\mu + k_1 (1 - 3\kappa)^2 (c^2 - s^2)^2}$$
(61)

Poisson's ratio v_{zy}

$$v_{zy} = \frac{4\mu + 8k_1(1 - 3\kappa)^2(c^2 - s^2)c^2}{8\mu + 8k_1(1 - 3\kappa)^2(c^2 - s^2)^2}$$
(62)

(57) Apply simple shear stress σ_{xy} to determine shear modulus G_{xy}

The deformation gradient and all related quantities to compute stress state in this loading case are:

$$F = \begin{bmatrix} 1 & \gamma & 0 \\ 0 & 1 & 0 \\ 0 & 0 & 1 \end{bmatrix}, \quad B = \begin{bmatrix} 1 + \gamma^2 & \gamma & 0 \\ \gamma & 1 & 0 \\ 0 & 0 & 1 \end{bmatrix},$$

$$C = \begin{bmatrix} 1 & \gamma & 0 \\ \gamma & 1 + \gamma^2 & 0 \\ 0 & 0 & 1 \end{bmatrix}$$
(63)

Other quantities in Eq. (50) for computing Cauchy stresses.

$$FL_{1} = \begin{bmatrix} 1 & \gamma & 0 \\ 0 & 1 & 0 \\ 0 & 0 & 1 \end{bmatrix} \begin{bmatrix} c \\ s \\ 0 \end{bmatrix} = \begin{bmatrix} c + s\gamma \\ s \\ 0 \end{bmatrix},$$

$$FL_{2} = \begin{bmatrix} 1 & \gamma & 0 \\ 0 & 1 & 0 \\ 0 & 0 & 1 \end{bmatrix} \begin{bmatrix} c \\ -s \\ 0 \end{bmatrix} = \begin{bmatrix} c - s\gamma \\ -s \\ 0 \end{bmatrix}$$
(64)

$$I_{41} = \begin{bmatrix} c & s & 0 \end{bmatrix} \begin{bmatrix} 1 & \gamma & 0 \\ \gamma & 1 + \gamma^2 & 0 \\ 0 & 0 & 1 \end{bmatrix} \begin{bmatrix} c \\ s \\ 0 \end{bmatrix}$$

$$= 1 + 2cs\gamma$$
(65)



$$I_{42} = \begin{bmatrix} c & -s & 0 \end{bmatrix} \begin{bmatrix} 1 & \gamma & 0 \\ \gamma & 1 + \gamma^2 & 0 \\ 0 & 0 & 1 \end{bmatrix} \begin{bmatrix} c \\ -s \\ 0 \end{bmatrix}$$

$$= 1 - 2cs\gamma$$
(66)

$$E_1 = (1 - 3\kappa)(2cs\gamma),$$

$$E_2 = (1 - 3\kappa)(-2cs\gamma)$$
(67)

$$FL_1 \otimes FL_1 = \begin{bmatrix} c + s\gamma \\ s \\ 0 \end{bmatrix} \begin{bmatrix} c + s\gamma & s & 0 \end{bmatrix}$$

$$= \begin{bmatrix} (c + s\gamma)^2 & s(c + s\gamma) & 0 \\ s(c + s\gamma) & s^2 & 0 \\ 0 & 0 & 0 \end{bmatrix}$$
(68)

$$FL_{2} \otimes FL_{2} = \begin{bmatrix} c - s\gamma \\ -s \\ 0 \end{bmatrix} \begin{bmatrix} c - s\gamma & -s & 0 \end{bmatrix}$$

$$= \begin{bmatrix} (c - s\gamma)^{2} & -s(c - s\gamma) & 0 \\ -s(c - s\gamma) & s^{2} & 0 \\ 0 & 0 & 0 \end{bmatrix}$$
(69)

Neglecting high order term of γ , the shear stress σ_{xy} in Eq. (33) becomes:

$$\sigma_{xy} = \left[2\mu + 8k_1(1 - 3\kappa)^2 c^2 s^2 \right] \gamma \tag{70}$$

Thus, the shear stress G_{xy} becomes:

$$G_{xy} = \frac{\sigma_{xy}}{\gamma} = 2\mu + 8k_1(1 - 3\kappa)^2 c^2 s^2$$
 (71)

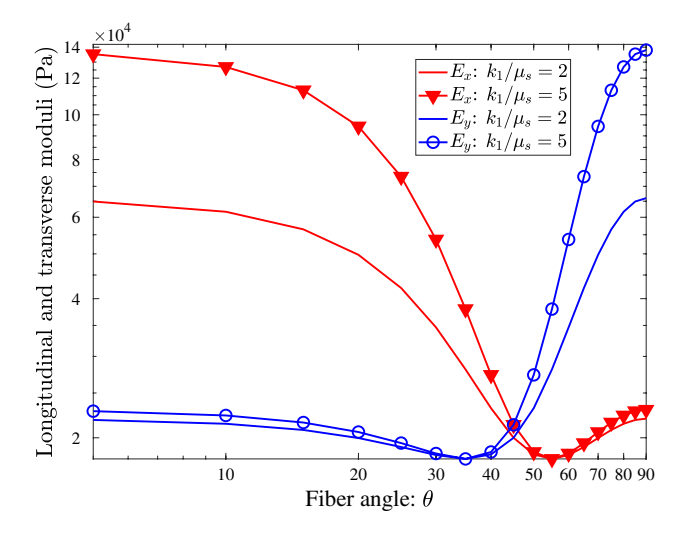


Fig. 17 Equivalent longitudinal and transverse moduli E_x , E_y versus fiber angle θ for the case of fiber dispersion $\kappa = 0$ in (x-y) fiber plane

With similar approach, the shear moduli G_{xz} , G_{yz} can also be determined. For fiber plane (x-y), these shear moduli are equal to the value of isotropic case $G_{yz} = G_{xz} = 2\mu$.

Figure 17 illustrates how the longitudinal (E_x) and transverse (E_y) stiffnesses vary with respect to the fiber angle θ at two values of fiber stiffness $k_1/\mu_s = 5$ and $k_1/\mu_s = 2$.

References

ABAQUS (2018) Analysis user's manual. Version 6.18. Dassault Systemes Simulia Inc., Providence, RI

Allen HJ (1969) Analysis and design of structural sandwich panels. Pergamon Press, Oxford

Annaidh AN, Bruyère K, Destrade M, Gilchrist MD, Maurini C, Otténio M, Saccomandi G (2012) Automated estimation of collagen fibre dispersion in the dermis and its contribution to the anisotropic behaviour of skin. Ann Biomed Eng 40:1666–1678

Biot MA (1963) Surface instability of rubber in compression. Appl Sci Res 12:168–182

Bowden N, Brittain S, Evans AG, Hutchinson JW, Whitesides GM (1998) Spontaneous formation of ordered structures in thin films of metals supported on an elastomeric polymer. Nature 393:146–149

Brangwynne CP, MacKintosh FC, Kumar S, Geisse NA, Talbot J, Mahadevan L, Parker KK, Ingber DE, Weitz DA (2006) Microtubules can bear enhanced compressive loads in living cells because of lateral reinforcement. J Cell Biol 173(5):733–741

Brau F, Vandeparre H, Sabbah A, Poulard C, Boudaoud A, Damman P (2011) Multiple-length-scale elastic instability mimics parametric resonance of nonlinear oscillators. Nat Phys 7:56–60

Cao Y, Hutchinson JW (2012) Wrinkling phenomena in neo-Hookean film/substrate bilayers. J Appl Mech 79(3):031019

Cardamone L, Valentin A, Eberth JF, Humphrey JD (2009) Origin of axial prestretch and residual stress in arteries. Biomech Model Mechanobiol 8(6):431–446

Cerda E (2005) Mechanics of scars. J Biomech 38:1598–1603

Cerda E, Mahadevan L (2003) Geometry and physics of wrinkling. Phys Rev Lett 90:074302

Chen L, Han D, Jiang L (2011) On improving blood compatibility: from bio-inspired to synthetic design and fabrication of biointerfacial topography at micro/nano scales. Colloids Surf B Biointerfaces 85:2-7

Ciarletta P, Izzo I, Micera S, Tendick F (2011) Stiffening by fiber reinforcement in soft materials: a hyperelastic theory at large strains and its application. J Mech Behav Biomed Mater 4:1359–1368

Ciarletta P, Balbi V, Kuhl E (2014) Pattern selection in growing tubular tissues. Phys Rev Lett 113:248101

Damman P (2015) Elastic instability and surface wrinkling. In: Rodriguez-Hernández J, Drummond C (eds) Polymer surfaces in motion: Unconventional patterning methods, Ch. 8. Springer, Heidelberg

de Rooij R, Kuhl E (2016) Consitutive modeling of brain tissue: current perspectives. Appl Mech Rev 68:010801/1-16

Epstein AK, Hong D, Kim P, Aizenberg J (2013) Biofilm attachement reduction on bioinspired, dynamic, micro-wrinkling surfaces. New J Phys 15:095018

Fraldi M, Palumbo S, Carotenuto AR, Cutolo A, Deseri L, Pugno N (2019) Buckling soft tensegrities: Fickle elasticity and configurational switching in living cells. J Mech Phys Solids 124:299–324



- Gasser TC, Ogden RW, Holzapfel GA (2006) Hyperelastic modelling of arterial layers with distributed collagen fiber orientations. J R Soc Interface 3(6):15–35
- Genzer J, Groenewold J (2006) Soft matter with hard skin: from skin wrinkles to templating and material characterization. Soft Matter 2:310–323
- Goriely A (2017) The mathematcis and mechanics of biological growth. Springer, Berlin
- Greensmith JE, Duling BR (1984) Morphology of the constricted arteriolar wall—physiological implications. Am J Physiol 247:H687–H698
- Hasan J, Chatterjee K (2015) Recent advances in engineering topography mediated antibacterial surfaces. Nanoscale 7:15568–15575
- Hill MR, Duan X, Gibson GA, Watkins S, Robertson AM (2012) A theoretical and non-destructive experimental approach for direct inclusion of measured collagen orientation and recruitment into mechanical models of the artery wall. J Biomech 45(5):762–771
- Hohlfeld E, Mahadevan L (2011) Unfolding the sulcus. Phys Rev Lett 106(105702):1-4
- Holzapfel GA, Ogden RW (2017) Biomechanics: trends in modeling and simulation. Springer, Berlin
- Holzapfel GA, Gasser TC, Ogden RW (2000) A new constitutive framework for arterial wall mechanics and a comparative study of material models. J Elast 61(1–3):1–48
- Levering V, Wang Q, Shivapooja P, Zhao X, Lopez GP (2014) Soft robotic concepts in catheter design: an on-demand fouling-release urinary catheter. Adv Healthc Mater 3:1588–1596
- Liu X, Yuan L, Li D, Tang Z, Wang Y, Chen G, Chen H, Brash L (2014) Blood compatible materials: state of the art. J Mater Chem B 2:5718–5738
- Mao C, Liang C, Luo W, Bao J, Shen J, Hou X, Zhao W (2009) Preparation of lotus-leaf-like polystyrene micro- and nanostructure films and its blood compatability. J Mater Chem 19:9025–9029
- Pocivavsek L, Dellsy R, Kern A, Johnson S, Lin B, Lee KYC, Cerda E (2008) Stress and fold localization in thin elastic membranes. Science 320:912–916
- Pocivavsek L, Leahy B, Holten-Andersen N, Lin B, Lee KYC, Cerda E (2009) Geometric tools for complex interfaces: from lung surfactant to the mussel byssus. Soft Matter 5:1963–1968

- Pocivavsek L, Pugar J, O'Dea R, Ye S-H, Wagner W, Tzeng E, Velankar S, Cerda E (2018) Topography-driven surface renewal. Nat Phys 14:948–953
- Pocivavsek L, Ye SH, Pugar J, Tzeng E, Cerda E, Velankar S, Wagner WR (2019) Active wrinkles to drive self-cleaning: a strategy for anti-thrombotic surfaces for vascular grafts. Biomateirlas 192:226–234
- Puntel E, Deseri L, Fried E (2011) Wrinkling of a stretched thin sheet. J Elast 105(1):137–170
- Rahmawan Y, Chen C-M, Yang S (2014) Recent advances in wrinklebased dry adhesion. Soft Matter 10:5028–5039
- Shivapooja P, Wang Q, Orihuela B, Rittschof D, Lopez GP, Zhao X (2013) Bioinspired surfaces with dynamic topography for active control of biofouling. Adv Mater 25(10):1430–1434
- Shyer AE, Tallinen T, Nerurkar NL, Wei Z, Gil ES, Kaplan DL, Tabin CJ, Mahadevan L (2013) Villification: how the gut gets its villi. Science 342:212–218
- Sidawy AN, Perler BA (eds) (2018) Rutherford's vascular surgery and endovascular therapy, 2 volume set, 9th edn. Elsevier, Amsterdam
- Stewart PS, Waters SL, El Sayed T, Vella D, Goriely A (2016) Wrinkling, creasing, and folding in fiber-reinforced soft tissues. Extreme Mech Lett 8:22–29
- Sun J-Y, Xia S, Moon M-W, Oh K-H, Kim K-S (2012) Folding wrinkles of a thin stiff layer on a soft substrate. Proc R Soc A 468:932–953
- Svendsen E, Tindall AR (1988) The internal elastic membrane and intimal folds in arteries: important but neglected structures? Acta Physiol Scand Suppl 572:1–71
- Vonach WK, Rammerstorfer FG (2000) The effects of in-plane core stiffness on the wrinkling behavior of thick sandwiches. Acta Mech 141(1-2):1-10
- Yang S, Khare K, Lin PC (2010) Harnessing surface wrinkle patterns in soft matter. Adv Funct Mater 20:2550–2564

Publisher's Note Springer Nature remains neutral with regard to jurisdictional claims in published maps and institutional affiliations.

